

JGR Earth Surface

RESEARCH ARTICLE

10.1029/2020JF005856

Key Points:

- A vegetation model was developed to simulate the impacts of multiple vegetation species on flow, turbulence, waves and sediment
- Three vegetation species were parameterized in the module, which was successfully applied to the tidal creek complex of Chongming Dongtan
- Model demonstrated seaward sediment export from creeks, and consistency between the predicted salinity and the vegetation zonation

Supporting Information:

Supporting Information may be found in the online version of this article.

Correspondence to:

J. Ge,
jzge@sklec.ecnu.edu.cn





Citation:

Ge, J., Yi, J., Zhang, J., Wang, X., Chen, C., Yuan, L., et al. (2021). Impact of vegetation on lateral exchanges in a salt marsh-tidal creek system. *Journal of Geophysical Research: Earth Surface*, 126, e2020JF005856. <https://doi.org/10.1029/2020JF005856>

Received 26 AUG 2020

Accepted 27 JUL 2021

Impact of Vegetation on Lateral Exchanges in a Salt Marsh-Tidal Creek System

Jianzhong Ge^{1,2} , Jinxu Yi¹, Jingting Zhang¹, Xianye Wang¹ , Changsheng Chen³ , Lin Yuan^{1,2}, Bo Tian¹, and Pingxing Ding¹ 

¹State Key Laboratory of Estuarine and Coastal Research, East China Normal University, Shanghai, China, ²Institute of Eco-Chongming (IEC), Shanghai, China, ³School for Marine Science and Technology, University of Massachusetts-Dartmouth, New Bedford, MA, USA

Abstract Salt marshes are ecologically and physically essential habitats in coastal intertidal flats. In addition to providing nursery grounds for various wildlife, vegetation in marshes acts as a buffer zone that slows flooding waters. Extensive marsh platforms can also attenuate wave energy to protect coastal communities. Complex geometries make it challenging for models to capture the spatiotemporal variabilities in the transport of lateral water and sediment over tidal creek-marsh complexes. To study water exchange processes between tidal creeks and marshes, field observations were conducted within tidal creeks in the Chongming Dongtan Shoal of the Changjiang Estuary, an area dominated by *Phragmites australis*, *Scirpus mariqueter*, and *Spartina alterniflora*. A coupled wave-current-sediment-vegetation model that parameterized the three vegetation species was developed and applied to the tidal creek complex of Chongming Dongtan. Validated with the observational data, the modeling results were used to examine the influence of vegetation on flooding/drainage processes within tidal creeks and mudflats. The model showed that vegetation not only modified the flow pattern at high tide in the high-elevation marsh but also significantly intensified the tidal flows in tidal creeks in the low-elevation regions. Both the observations and model detected significant transport of water and sediment from the marsh to tidal creeks, seaward sediment export over tidal cycles. The simulated salinity exhibited a considerable spatial gradient, matching well with the salt tolerances of the major vegetation types. This model can be potentially used to determine how future scenarios of hydrodynamics could affect vegetation zonation.

1. Introduction

Coastal salt marshes are characterized by vegetated platforms that are regularly flooded with tidal water delivered through a network of channels (Chirol et al., 2018; Lacy et al., 2018; McOwen et al., 2017; Xie et al., 2018). Vegetation in salt marshes significantly increases the sediment capture efficiency in highly turbid estuarine environments (Field et al., 2012; Larsen, 2019). Intertidal flat, defined as the area between the average lowest and highest sea water level at low tide and high tide, usually consists of bare mudflats in low-elevation forelands and vegetated salt marshes in high-elevation areas. Tidal creeks flow through most marshes, connecting with adjacent coastal and estuarine waters. Salt marsh vegetation provides nursery grounds for a wide range of wildlife (Boesch & Turner, 1984; Katul et al., 2011).

Resolving and accurately simulating water exchange in tidal creek-salt marsh complexes comprise fundamental modeling problems; the water exchange process involves a lateral flow process driving the residual transport of water, salinity, sediments, and nutrients (Chu et al., 2018; Poepl et al., 2016; Schuerch et al., 2014; Serra et al., 2004; Wang et al., 2016). It is well recognized that emergent, flexible or rigid vegetation in salt marshes functions as stem-exerted drag throughout the entirety or part of the water column. Vegetation-induced drag can slow flows, enhance flow asymmetry over tidal cycles (De Serio et al., 2018; Folkard, 2011; Hu et al., 2015; Luhar & Nepf, 2011; Nepf & Vivoni, 2000; Nepf, 2012), deplete wave energies (Heuner et al., 2015), increase the vertical shear of horizontal flow, and intensify vertical mixing (Nepf, 1999; Tanino & Nepf, 2008). Small-scale interactions among vegetation, flow, and sediment in regular shape can be accurately represented by numerical models, as shown in flume experiments (Ma et al., 2014; Marsooli and Wu et al., 2014; Yang et al., 2017). However, due to irregular geometries in tidal creeks and the presence of various salt marsh plant species, it is challenging to numerically capture lateral transport in

tidal creek-salt marsh systems. Vegetation in these areas usually has different spatial coverage, from small patches of only several meters to large coverage of several kilometers (Larsen, 2019). Vegetation patches and tidal creeks with various horizontal scales can significantly influence the lateral transport of water and sediment, resulting in sediment accumulation and geomorphological change over local to regional scales (Coco et al., 2013; Donatelli et al., 2018; Houwing, 1999; Larsen, 2019; Shi et al., 2017a; Stefanon et al., 2010; Tal & Paola, 2010; Xie et al., 2018; Yu et al., 2017). In turn, vegetation growth and degradation in salt marshes are significantly altered by dissolved nutrients and particulate matter laterally transported between tidal creeks and salt marshes (Chu et al., 2018; Larsen, 2019). Moreover, sediment transport is highly influenced by spatial settling lags, which are extensively modified by various vegetation types through turbulence-induced vertical mixing (Coleman et al., 2020; Leonard & Reed, 2002).

Tidal creeks are a major water pathway that floods into and drains out from salt marshes (Chen et al., 2008; Coleman et al., 2020; Donatelli et al., 2018; Kirwan et al., 2011; Mariotti, 2018; Mariotti & Fagherazzi, 2012, 2013). Lateral water, salinity, and sediment transport in tidal creek-salt marsh complexes are driven by nonlinear interaction processes, which vary significantly with the coverage of plant species, distance from the marsh edge, and flow intensity in the tidal creeks. The flows are predominantly stronger inside tidal creeks than in nearby mudflats. Impulse-like alternating ebb and flood flows are often observed at the edges of tidal creeks and mudflats (Shi et al., 2017a; Xie et al., 2018); these flows can modify flood-ebb dominance over a distance, affect the vegetation types, and excite geometrically controlled eddies. Asymmetric flows and eddies vary significantly with salt marsh elevation, geometric shape of the creek, and tidal intensity and phase (Chen et al., 2008; Lacy et al., 2018; Poirier et al., 2017). It is difficult to accurately estimate these transports by either field measurements with limited coverage or by models that do not resolve vegetation.

To resolve the spatial features of vegetation patches and tidal creeks with a degree of geometrical irregularity on the order of <1.0 m to several kilometers, one requires a multiscale-resolving numerical model capable of discretizing meshes with a resolution up to a few meters (Chen et al., 2008; D'Alpaos et al., 2019; Mariotti, 2018; Temmerman et al., 2005; Verschelling et al., 2017). This model needs to consider the effects of vegetation on flows, mixing, waves, and sediments (Baptista et al., 2005; Klopstra et al., 1997). Beudin et al. (2017) developed a comprehensive structured grid, wave-flow-vegetation, interaction model. An unstructured-grid model, for example, the finite-volume community ocean model (FVCOM), can resolve complex irregular coastal and estuarine geometries. The FVCOM has been successfully applied to simulate water changes over tidal creek-salt marsh complexes with high resolutions of up to a few meters in coastal regions encompassing salt marshes (e.g., Chen et al., 2008, 2013; Ge et al., 2015, 2018, 2020; Lai et al., 2015; Zhao et al., 2010).

This study implemented vegetation physics in the FVCOM and upgraded the model into a fully coupled wave-flow-vegetation-sediment model. We applied this model to simulate tidal flows, salinity, and sediment over a tidal creek-salt marsh complex in the Chongming Dongtan Shoal of the Changjiang Estuary. This study focused on assessing the spatiotemporal patterns of salinity transport and their link to the salt tolerance of the major vegetation types in the salt marsh tidal creek system under various tidal conditions. A series of process-oriented numerical experiments with/without vegetation were then performed to qualify the critical contributions of vegetation to the water, salinity, and sediment transport processes between salt marshes and tidal creeks.

2. Study Area, Data, and Model

2.1. Study Area

The tidal creek-salt marsh complex around Chongming Dongtan was selected as the study area. Chongming Dongtan is located on the eastern side of Chongming Island in the Changjiang River (Figure 1). The area encompasses the largest estuarine salt marsh in the Changjiang River Estuary and is protected as the Chongming East Shoal Nature Reserve (Xie et al., 2018).

As viewed from a 10-m-resolution remote sensing image produced by the Sentinel-2 satellite, Chongming Dongtan features a broad salt marsh with fully developed massive tidal creeks, bare mudflats, and extensive vegetation coverage (Figure 1a). The central portion of the salt marsh covers approximately 18.37 km²,

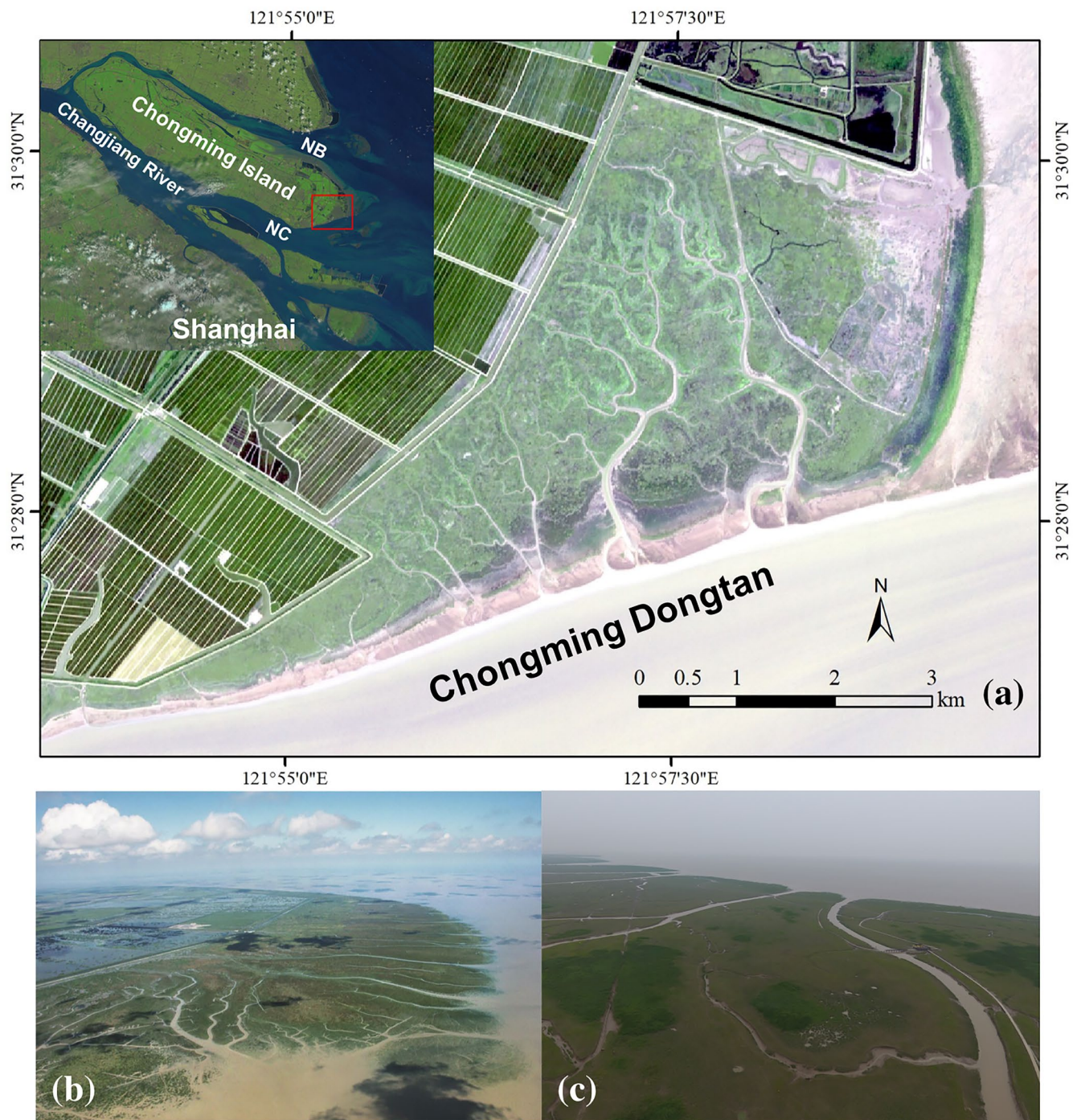


Figure 1. Location and overview of Chongming Dongtan, including salt marsh and tidal creeks. (a) Image retrieved from remote sensing images of the Sentinel-2 satellite; (b) an aerial view of vegetation, marshes, and creeks from an image captured by an unmanned aerial vehicle (UAV); and (c) an enlarged view of a selected area from the UAV image. NC and NB in (a) indicate the North Channel and North Branch, respectively.

with a landscape gradient of 0.2%–0.5%. Previous observations have revealed that some relatively deeper mudflat areas are dominated by small-scale, eddy-like flows that are influenced by alternating tidal ebb and flood flows (Wang et al., 2011). In the river mouth (Figure 1a), the tidal range is approximately 4.6 m, with a maximum amplitude of ~2.6 m. The Changjiang River Estuary is highly turbid with a suspended sediment concentration (SSC) of ~0.5–5 g/L in the water column inside the river and of 0.1–6 g/L in the salt marsh (Ge et al., 2015; Shi et al., 2017b; Xie et al., 2018). The river flow transports abundant sediment

into the estuarine region, resulting in a maximum lateral progradation rate of 352 m/yr around Chongming Dongtan (Yang et al., 2001). In the last decade, the terrestrial sediment load from the Changjiang River has significantly decreased due to the operation of the Three Gorges Dam. However, the sedimentation rates remain high in the salt marsh around Chongming Dongtan (Luan et al., 2016).

A variety of vegetation (26 species in total) grows in Chongming Dongtan, with the three dominant species including *Phragmites australis*, *Scirpus mariqueter*, and *Spartina alterniflora*. These plants cover most areas of Chongming Dongtan (Figure 1b). The *S. mariqueter* community is mainly distributed in areas with elevations of >0.3 m above mean sea level (Yuan et al., 2014). The *P. australis* and *S. alterniflora* communities are distributed in areas with elevations of >0.9 and 1.3 m above mean sea level, respectively (Cui et al., 2020). These species' distributions are highly dynamic, with their spatial coverages varying annually (Yuan et al., 2014).

The tidal creeks in the study area are well developed, with spatial widths in the range of ~1 m to several hundred meters (Figure 1c). These creeks are highly fractal, with several branches spanning from the entrance near the river mouth to the end of the salt marsh near the dikes (Figure 1a). The maximum width at the entrance is ~280 m, located near the center of Chongming Dongtan. These tidal creeks feature energetic water discharges during flood and ebb tides, a primary physical process that drives sediment suspension and transport. According to field measurement data, the tidal-averaged SSC in the creek is 0.26–1 g/L. The SSC can reach ~2–6 g/L at its peak, occurring near the bottom of the marsh during the early flood tidal period (Xie et al., 2018).

The Changjiang River Estuary splits into the North Channel and North Branch near Chongming Dongtan (Figure 1a). The North Channel is an interactive region between riverine freshwater and oceanic saltwater and is influenced significantly by freshwater-induced river flows, tidal currents, and oceanic inflows (Xue et al., 2009). In the wet summer season, the river freshwater discharge is high, reaching >40,000 m³/s. The estuarine region around Chongming Dongtan is vertically stratified, with low-salinity riverine water near the surface and high-salinity oceanic water near the bottom. As a result, Chongming Dongtan is surrounded by residual flows circulating from the North Channel to the North Branch. In the dry winter season, the stratification is relatively weak due to low freshwater discharge. The North Channel is often occupied by saltwater intruded from the ECS nearshore (Xue et al., 2009), and the residual flows could be the opposite in winter compared with those in summer. The salinity varies significantly around Chongming Dongtan. At the southern edge, the salinity is ~0.2 PSU in the summer and ~0.4 PSU in the winter (Cheng et al., 2015). In August 2018, we performed a salinity measurement on the northern side of the salt marsh at 20 cm above the bed using a conductivity and temperature recorder (model type: SBE CTD 37-SMP) with 3-min sampling interval, and obtained values of ~4–18 PSU.

2.2. Data

2.2.1. Bathymetry

A Riegl VZ-4000 terrestrial laser scanner (TLS) was used to acquire high-resolution bathymetry data across Chongming Dongtan. This scanner's maximum-reaching range is up to 4 km, with an uncertainty of 0.01–0.03 m (Riegl, 2019). Xie et al. (2017) performed extensive TLS measurements around Chongming Dongtan. The vegetation height was removed from the raw scanned point cloud data, and the ground elevation was determined through progressive morphological filtering. In 2015, TLS measurements were used to determine the bathymetry of the entire Chongming Dongtan region. The raw bathymetry data were post-processed with a spatial resolution of 0.05 m using a digital elevation model (DEM). This resolution was sufficient to meet the requirements for numerical modeling. The TLS-produced bathymetry data accurately captured the elevations in bare mudflats and the salt marsh (Figure 2a), which is particularly important for the bathymetric boundary between the salt marsh and tidal creeks. However, the TLS was not able to accurately measure the bathymetry in the tidal creeks. Instead, a waterline method combining remote sensing images and a hydrodynamic model was chosen to construct the bathymetry in these regions. This method was developed and used by Zheng et al. (2007). The elevations in the mudflats were within the range of 1.0–2.5 m. The tidal creeks were relatively deeper in areas close to the creek entrances and gradually became shallower in the high-elevation intertidal flats.

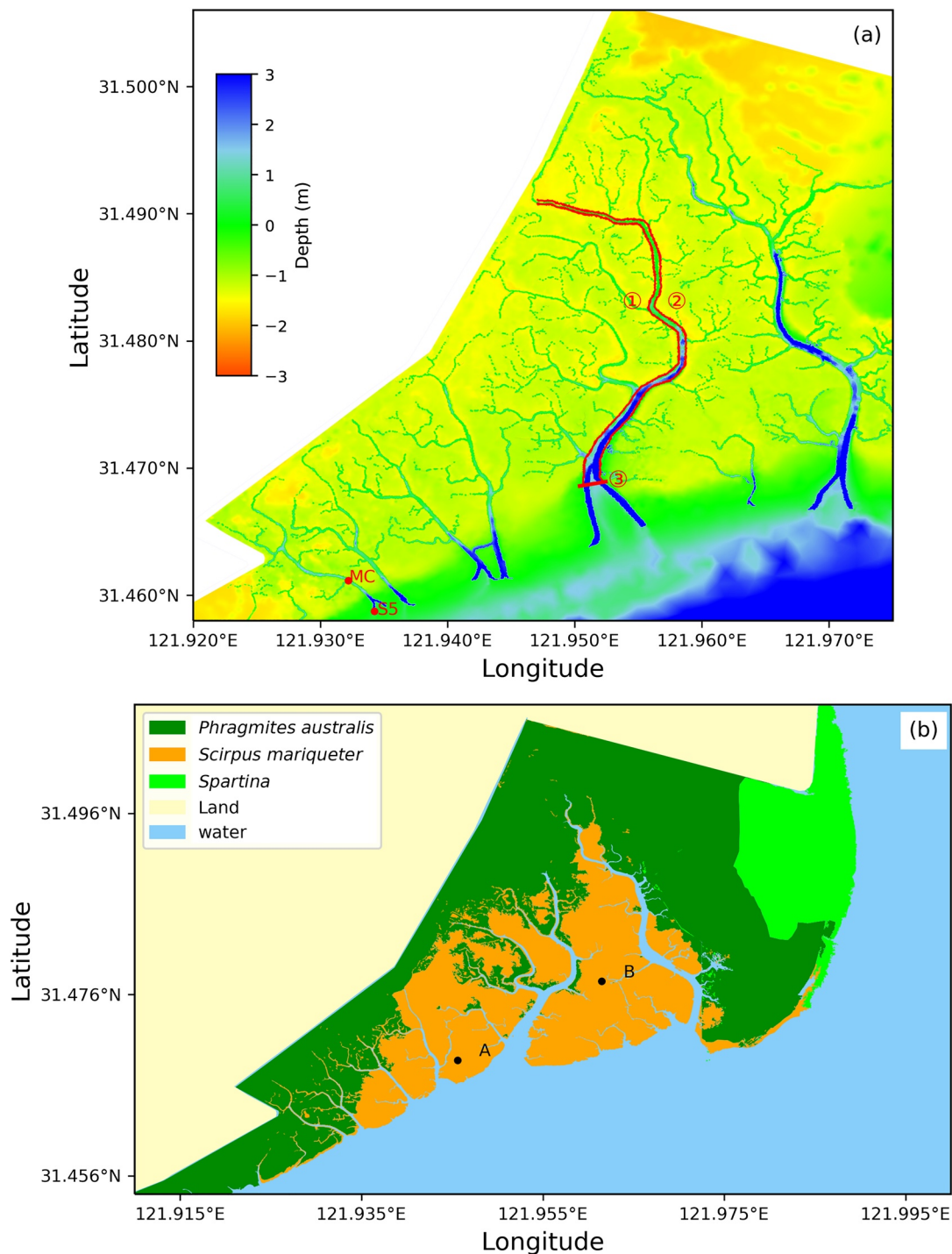


Figure 2. Bathymetry and vegetation coverage of the study area. (a) Bathymetry of Chongming Dongtan, retrieved by a terrestrial laser scanner (TLS) system. The water elevation and flow velocities were measured at site MC, and the suspended sediment concentration was monitored at site S5. The two irregular curves (lines 1 and 2) indicate the two lateral boundaries along the middle tidal creek, and line 3 shows the outer edge. (b) The spatial distributions of the vegetation coverages of *Spartina alterniflora*, *Scirpus mariqueter*, and *Phragmites australis* in Chongming Dongtan in September 2015. Black bullets in panel b indicate the selected sites.

2.2.2. Vegetation

Multispectral Pleiades remote sensing data, collected on September 12, 2015 were used to specify the spatial coverages of vegetation species. These data were processed using the ENVI 5.1 Imagine software (Harris

Geospatial Solutions, Inc., USA) and geometrically calibrated using a 1:10,000-ratio nautical chart. The snapshot was taken with a resolution of 0.5 m close to the low tide, where the water boundary was far from any vegetation. The interpretation was performed using the tasseled cap (K-T) transform spectral enhancement method combined with the normal difference vegetation index (NDVI) (Huang & Zhang, 2007). Based on the reliable ground information obtained from a preconduted field survey, a set of classes (water, mud-flat, dike, *S. alterniflora*, *S. mariqueter*, and *P. australis*) were identified and selected as training samples. A supervised classification technique using the maximum likelihood classifier in ENVI Imagine software was first performed (Karan & Samadder, 2016). In situ field verifications were then conducted to validate the results of the image classification. The classified images were integrated into a geographic information system (GIS) platform to analyze the spatial dynamics of the salt marsh vegetation types in Chongming Dongtan.

The spatial distributions of the three major vegetation types are shown in Figure 2b. Similar to the general distribution pattern described in Figure 1b, *P. australis* mainly covered an area spanning from the high-elevation salt marsh to the dikes. *S. alterniflora* was only distributed in the northeastern region of the study area. *S. mariqueter* was generally found in the low-elevation intertidal flats and was distributed as scattered patches within *P. australis* stands (Figure 2b).

2.2.3. Measurement Data

We set up two monitoring stations at sites MC and S5 to measure currents and water levels (Figure 2a). These two sites were placed in low- and mid-elevation central areas of a tidal creek. These two areas were bounded by a mixture of *P. australis* and *S. mariqueter*. Moreover, this creek was close to land, allowing the field deployment and retrieval of observational instruments to be relatively more straightforward. Water currents were measured using an acoustic Doppler velocimeter (ADV; Nortek AS, Norway) with a sensor at a height of 30 cm above the creek bed. The sampling interval for ADV was set to 10 min, with a sampling frequency of 16 Hz and a duration of 70 s. The water level was recorded by RBR Tide & Wave Loggers (RBR, Limited, Canada) with a sampling interval of 5 min. At site S5, an optical backscattering sensor (OBS) was mounted at a depth of 25 cm above the creek bed to measure water turbidity. Water turbidity was converted to the suspended sediment concentration through laboratory calibration. Sediment samples collected at site S5 were placed in a rotating water tank in the laboratory to produce various turbidity levels, and the synchronously turbid water in the tank was measured to determine the actual sediment concentration. Through this method, the regression function of water turbidity against the suspended sediment concentration was constructed with $R^2 > 0.95$, indicating a reliable fitting. The ADV sensor sampling interval was also set to 10 min. The measurements started at 8:00 p.m. on September 12, 2015 and lasted until 10:55 a.m. on September 23, 2015. These data were mainly used for model validation.

2.3. Model Development

The FVCOM version used in this study included the flow-vegetation-wave-sediment interaction process. FVCOM is a prognostic, unstructured-grid, finite-volume, free-surface, three-dimensional (3-D) primitive equation community ocean model developed by Chen et al. (2003) and has subsequently been upgraded with contributions from user communities (Chen et al., 2013). The model uses generalized terrain-following coordinates and contains a wet/dry treatment for flooding and draining. Spatial discretization in the FVCOM is performed using nonoverlapping triangular meshes; this method provides accurate geometrical fitting for irregular vegetation patches and tidal creeks. The finite-volume scheme used in the FVCOM guarantees optimal conservation of mass, momentum, salt, and sediment in coastal and estuarine regions. The FVCOM is widely used for coastal and estuarine simulations (Chen et al., 2008). Details of FVCOM modules are described in the FVCOM User Manual (Chen et al., 2013). Here, a brief description is given for the vegetation module.

2.3.1. Effects of Vegetation on Currents and Waves

In a dynamic wave-vegetation-sediment interaction system, vegetation acts as a drag force for both currents and waves. F_x and F_y are defined as the x - and y -components of the source and sink forcing terms in the momentum equations. These two terms are given as follows:

$$F_x = F_{r,x} + F_{d,veg,x} + F_{s,veg,x} \quad (1)$$

$$F_y = F_{r,y} + F_{d,veg,y} + F_{s,veg,y} \quad (2)$$

where F_r , $F_{d,veg}$, and $F_{s,veg}$ are the wave-averaged, vegetation-induced drag, and in-canopy wave-induced streaming forces, respectively. Subscripts x and y represent the x and y components, respectively. F_r has previously been included as a three-dimensional (3D) wave radiation stress factor in the FVCOM (Niu & Xia, 2017; Wu et al., 2011). $F_{d,veg}$ and $F_{s,veg}$ can be calculated using the Beudin et al. (2017)' empirical formulas, given as follows:

$$F_{d,veg} = \frac{1}{2} C_D b_v n_v \bar{v} \sqrt{u^2 + v^2} \quad (3)$$

$$F_{s,veg} = \frac{S_{d,veg} \tilde{k}}{\rho_0 \tilde{\sigma}} \quad (4)$$

where C_D is the vegetation drag coefficient, specified as a constant under the assumption of a high Reynolds number; b_v is the stem width for an individual vegetation type; n_v is the vegetation density calculated with the number of stems per unit area; u and v are the x - and y -components of the horizontal velocity at each vertical layer in a canopy with a height l_v , respectively; \bar{v} is the vector of the horizontal velocity at each vertical layer; \tilde{k} is the wavenumber; and $\tilde{\sigma}$ is the average wave frequency. $S_{d,veg}$ is the wave-induced streaming observed within the canopy and is associated with the direction of wave propagation (Luhar & Nepf, 2013; Luhar et al., 2010). We adopted the formula from the structured-grid ROMS and converted it to an unstructured grid algorithm for the FVCOM. $S_{d,veg}$ represents the total wave energy dissipation due to vegetation and can be calculated in the wave module in the FVCOM (Qi et al., 2009) as follows:

$$S_{d,veg} = -\sqrt{\frac{2}{\pi}} g^2 \tilde{C}_D b_v n_v \left(\frac{\tilde{k}}{\tilde{\sigma}} \right)^3 \frac{\sinh^3(\tilde{k} l_v) + 3 \sinh(\tilde{k} l_v)}{3 \tilde{k} \cosh^3(\tilde{k} h)} \sqrt{E_{tot}} E(\sigma, \theta) \quad (5)$$

where \tilde{C}_D is the bulk drag coefficient dependent on wave height, h is the total water depth, E_{tot} is the total wave energy, and $E(\sigma, \theta)$ is the wave energy at frequency σ and direction θ .

When the vegetation in the salt marsh is flexible, the bending of the plant stems can reduce vegetation drag. Following the methods of Luhar and Nepf (2011), a generally applicable algorithm was implemented to determine the effective blade height l_{ve} . Defining l_v as a flexible blade height, l_{ve} can be determined by the following formula:

$$\frac{l_{ve}}{l_v} = 1 - \frac{1 - 0.9 C_a^{-1/3}}{1 + C_a^{-3/2} (8 + B^{3/2})} \quad (6)$$

where C_a is the Cauchy number and B is the buoyancy parameter. These values are defined as follows:

$$C_a = 0.5 \frac{\rho C_D b_v U^2 l_v^3}{EI} \text{ and } B = \frac{(\rho - \rho_v) g b_v t_v l_v^3}{EI} \quad (7)$$

where I is the inertia moment of the blade area, treated as a rectangular section; t_v is the blade thickness; E is Young's modulus (elasticity); ρ_v is the stem tissue density; and $U = \sqrt{u^2 + v^2}$.

2.3.2. Effects of Vegetation on Turbulence

The FVCOM supports many oceanic turbulence closure models, including the Mellor and Yamada (1982) level 2.5 (MY2.5) turbulence closure model. Following the methods of Uittenbogaard (2003), we added vegetation-induced turbulence production (P_{veg}) and dissipation (D_{veg}) into the MY2.5 model in the FVCOM as follows:

$$P_{veg} = \sqrt{(F_{d,veg,x}u)^2 + (F_{d,veg,y}v)^2} \text{ and } D_{veg} = c_2 \frac{P_{veg}}{\tau_{eff}} \quad (8)$$

where τ_{eff} is defined as the minimum between the dissipation timescale of free turbulence and the timescale of eddies among the vegetation. The term τ_{eff} can be calculated as follows:

$$\tau_{eff} = \min(\tau_{free}, \tau_{veg}) \quad (9)$$

where $\tau_{free} = q^2 / \varepsilon$, $\tau_{veg} = \left(\frac{L^2}{c_k^2 P_{veg}} \right)^{1/3}$, $L(z) = c_l \left(\frac{1 - b_v t_v n_v}{n_v} \right)^{1/2}$, $c_k \approx 0.09$, L is the typical distance between two canopies, and c_l is a coefficient of order unity.

2.3.3. Effects of Vegetation on Sediments

The FVCOM encompasses the sediment module with options of either noncohesive or cohesive sediments (Chen et al., 2013; Ge et al., 2015). After defining C_i (g/L) as the SSC of the i th sediment group in the water column, the governing advection-diffusion equation for C_i can be expressed as follows:

$$\frac{\partial C_i}{\partial t} + \frac{\partial u C_i}{\partial x} + \frac{\partial v C_i}{\partial y} + \frac{\partial (w_i - w_s) C_i}{\partial z} = \frac{\partial}{\partial x} \left(A_H \frac{\partial C_i}{\partial x} \right) + \frac{\partial}{\partial y} \left(A_H \frac{\partial C_i}{\partial y} \right) + \frac{\partial}{\partial z} \left(K_h \frac{\partial C_i}{\partial z} \right) \quad (10)$$

where w_i (m/s) is the corresponding settling velocity and A_H and K_h are the horizontal and vertical eddy viscosities, respectively; these values are determined by the MY2.5 model in the FVCOM. In the vegetated water column, A_H and K_h include the vegetation-produced turbulences given by Equations 8–9.

As a default setup, cohesive sediment is transported by advection and mixed by diffusion, satisfying Equation 10. The balance between shear stress-dependent erosion and floc-size-dependent settling velocities follows the *Partheniades-Krone* equation. This equation is widely used in estuaries (Partheniades, 1965). Recent studies have revealed that sediment transport models that are based on bed shear stress (τ_b) may not capture the physical processes in vegetated areas where the bed-load sediment is energetic (Tinoco & Coco, 2018; Yang et al., 2016; Yang & Nepf, 2018). In these areas, the incipient motion of the bed and suspended loads are mainly controlled by a threshold value of the turbulent kinetic energy (k_t) rather than by τ_b . In vegetated areas, the bed-load sediment transport rate (Q_s) can be calculated using the formula of Yang and Nepf (2018):

$$Q_s = \begin{cases} 2.15 e^{-2.06/k_{t*}}, & k_{t*} < 0.95 \\ 0.27 k_{t*}^3, & 0.95 < k_{t*} < 2.74 \end{cases} \quad (11)$$

where $k_{t*} = \frac{k_t}{(\rho_s / \rho - 1) g d_s}$ and d_s is the median grain size. The term k_t can be determined as follows:

$$k_t = \left(\frac{C_f}{0.19} + 0.9 C_D^{2/3} \phi^{2/3} \right) U^2 \quad (12)$$

where C_f is the bed drag coefficient; $C_D \approx 1$ (Nepf, 1999); and $\phi = (\pi/4) n d^2$ is the solid volume fraction of the vegetation, where d is the vegetation canopy diameter and n is the number of vegetation stems per square meter.

The threshold velocity for the incipient motion of bed-surface sediment in the vegetated areas can be calculated using the following equation:

$$\frac{U_{crit}}{U_0} = \frac{1}{\sqrt{1 + C \phi^{2/3}}} \quad (13)$$

where $U_0 = \sqrt{\tau_{ci} / \rho C_b}$ is the critical velocity for a bare mudflat for a specific sediment class; $U_{crit} = U_0$ when there is no plant presence ($\phi = 0$); and $C = 0.9 C_D^{2/3} / C_b$, C_b is the coefficient dependent on bed roughness (Yang et al., 2016). For dense vegetation, U_{crit} has a weaker dependence on ϕ than in areas with sparse vegetation (Tanino & Nepf, 2008).

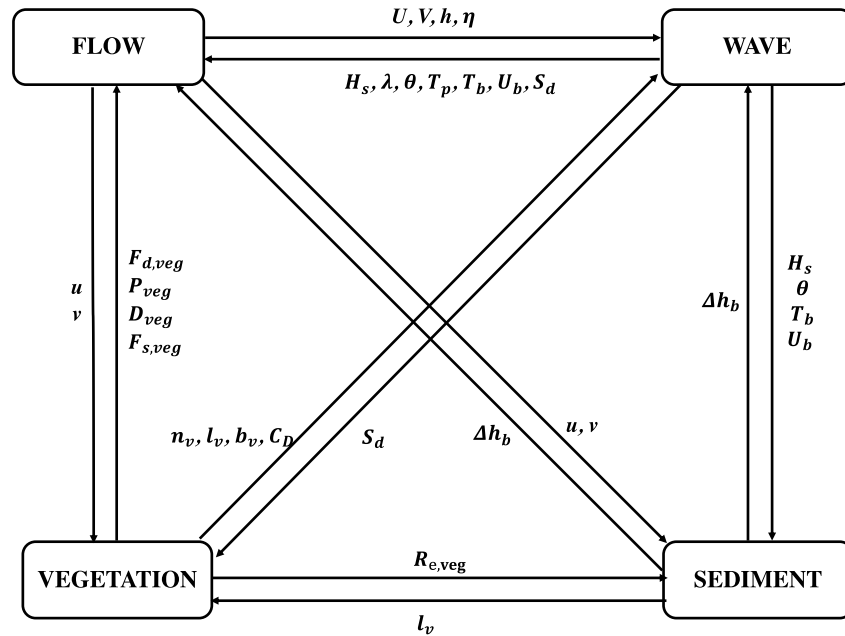


Figure 3. Data exchanges among the flow, wave, sediment, and vegetation modules during the dynamic interaction procedure.

Vegetation also influences sediment deposition. The experiments of Liu and Nepf (2016) indicated that a canopy Reynolds number (Re_d) equaling 120 can serve as the threshold value. Below this value, stem-induced turbulence is eliminated, meaning deposition increases. Above this value, stem-induced turbulence is generated, restricting sediment deposition. Re_d can be estimated by $Re_d = ud / \nu$, where u is the water velocity within vegetation; d is the stem diameter; and ν is the kinematic viscosity.

The bedload and suspended load transport equations are chosen for modeling based on the landscape-type specification. When vegetation is considered, Equations 10 and 12 are turned on in the sediment calculation. In mudflats and tidal creeks where vegetation is absent, the *Partheniades-Krone* equation is used for suspended load transport, and the *Meyer-Peter-Müller* formulation is chosen for bedload transport. The original and default settings in the FVCOM sediment module include these formulations (Chen et al., 2013; Ge et al., 2015, 2020; Warner et al., 2008).

2.3.4. Flow-Vegetation-Wave-Sediment Coupling

We coupled the vegetation module with flow-wave-sediment modules in the FVCOM. This coupling was approached without the need for an external coupling toolkit since all components shared the same grid. The data exchange among these modules is shown in Figure 3. The three-dimensional (3D) flow module delivers the depth-averaged flow velocities (U, V), depth (h), and sea surface elevation (η) to the wave module. It also provides flow velocities (u, v) in vertical layers to the vegetation module. The vegetation module sends the vegetation plant drag coefficient (C_D), stem width (b_v), vegetation density (n_v), and canopy height (l_v) values to the wave module and returns with the vegetation-induced wave damping ($S_{d,veg}$) values. The wave module forwards the significant wave height (H_s), wavelength (λ), wave direction (θ), peak period (T_p), bottom orbital period (T_b), bottom orbital velocity (U_b), and wave energy dissipation (S_d) information to the flow module. The vegetation module dispatches the vegetation-induced drag force ($F_{d,veg}$), turbulence production (P_{veg}), and dissipation (D_{veg}) due to vegetation to the flow module. It also sends the canopy Reynolds number (Re_d) to the sediment module and returns with the updated canopy height (l_v) for cases in which significant deposition-induced burial or erosion-induced exposure (Δh_b) exists. Other data exchanges among flow, waves, and sediment are described in Wu et al. (2011).

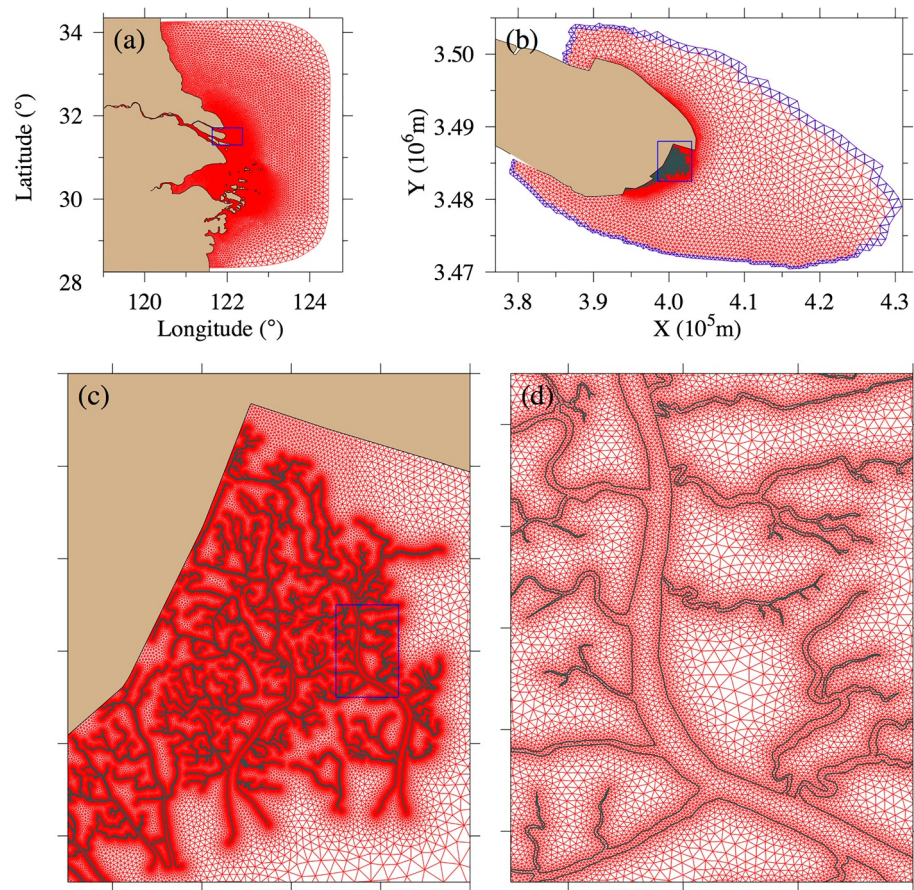


Figure 4. Model domains. (a) Large domain mesh covering the Changjiang River Estuary and adjacent coastal regions, (b) small domain mesh around Chongming Dongtan, (c) an enlarged view of the salt marsh, and (d) an enlarged view of a selected creek. Each blue rectangle in (a), (b), and (c) indicates the domain chosen for the enlarged views. The gray curves in (c) and (d) are the boundaries of tidal creeks. The blue triangles in (b) indicate the nesting boundary.

2.3.5. Model Configuration

The model was configured with two nesting computational domains covering the region from the Changjiang River Estuary to Chongming Dongtan (Figure 4). The large domain covered the Changjiang River Estuary and its adjacent nearshore areas (Figure 4a). The grid used for this domain was adopted from Ge et al. (2013). The small domain covered Chongming Dongtan with a refined resolution in tidal creeks and salt marshes (Figures 4b–4d). These two domains were connected at each vertical level through one-way nesting of boundary cells and nodes (blue triangles in Figure 4b). Both domains were constructed with triangular meshes. The meshes in the small domain were generated using the MATLAB-based DistMesh algorithm (Supporting Information S1). The horizontal resolution varied in the range of ~5 m in tidal creeks and up to ~20–40 m in the nearby mudflats. In the vertical direction, both the small and large domains were vertically discretized into 10 uniform sigma layers.

The high-resolution bathymetry data were interpolated into the mesh of the small domain. Typical stem density (n_v), upright stem height (l_v), stem width (b_v), and blade thickness (t_v) values were specified for the three major plant species, *S. alterniflora*, *S. mariqueter*, and *P. australis*, as listed in Table 1. The elasticity modulus (Young's modulus) was determined by Zhu et al. (2019). This modulus shows that *P. australis* has a much higher stiffness than the other two vegetation types, suggesting that rigid characteristics are more significant during shallow submergence. The flexibility of this vegetation type may only be notable under high or full submergence. *S. alterniflora* and *S. mariqueter* are typically flexible vegetation and have smaller elasticity values than *Phragmites*.

Table 1
Vegetation Parameters in Chongming Dongtan

Plant type	n_v (stems/m ²)	l_v (m)	b_v (m)	t_v (m)	E (GPa)
<i>Spartina</i>	127	1.517	0.005	0.0005	57
<i>Phragmites</i>	107	1.589	0.007	0.0007	753
<i>Scirpus</i>	627	0.611	0.003	0.0003	12

The model was driven by tidal elevations at the open boundary of the large domain, meteorological forcing at the surface, and river freshwater discharge at the upstream end; it was initialized with 3D fields of temperature and salinity and integrated with a mode-splitting time scheme. The time steps for the external and internal modes were 1.0 and 10.0 s in the large domain and 0.1 and 1.0 s in the small domain, respectively. The time step of 10 min used for the wave module was the same as that used by Ge et al. (2013, 2020). Meteorological forcing was constructed using ERA-Interim data from the European Center for Medium-Range Weather Forecasts. The daily river discharge was obtained from the Changjiang River boundary at the Datong station. Tidal forcing was predicted from the TPXO 8 database (Egbert & Erofeeva, 2002). The other configurations used in the large domain were the same as those applied by Ge et al. (2015, 2020). To examine the impacts of vegetation on physical processes in the tidal creek-salt marsh complex, we ran the model with and without the inclusion of vegetation.

Since the sediment in Chongming Dongtan and the adjacent Changjiang River Estuary is mainly dominated by fine cohesive dynamics, the sediment model in this study was configured as a cohesive type. The critical shear stress for erosion was specified as 0.2 N/m² in the bare mudflat and water region without vegetation and 0.05 N/m² in the tidal creeks. Following Ge et al. (2015), the erosion rate was set to 2.0×10^{-4} kg/m²/s. The median grain size (d_s) was 0.008 mm, and the settling velocity of sediment particles was set to 0.7 mm/s. Previous observations have indicated that the suspended sediment concentrations of mud are >10 g/L in tidal creeks and 1–2 g/L in intertidal mudflats (Shi et al., 2017b; Xie et al., 2018). Under high SSC conditions, hindered settling could become essential for reducing the effective settling velocity. This hindered settling of fine cohesive sediments can be calculated by the following equation:

$$w_s = w_{s,0} \frac{(1 - \phi_*) (1 - \phi_p)}{1 + 2.5\phi} \quad (14)$$

where $w_{s,0}$ indicates the settling velocity in clear water; w_s is the hindered settling velocity; $\phi = c / c_{gel}$ is the volumetric concentration; c and c_{gel} are the sediment mass concentration and gelling concentration, respectively; ϕ_p is the volumetric concentration of primary particles; and $\phi_* = \min\{1, \phi\}$. Equation 14 was adopted from Winterwerp and Van Kesteren (2004).

Moreover, a high-concentration mud suspension also affects the turbulent kinetic energy and K_h (Ge et al., 2018; Geyer, 1993), which can be determined by using the Richardson number-dependent formulation proposed by Munk and Anderson (1948) as follows:

$$K = K_0 \left(1 + \frac{10}{3} Ri \right)^{-1.5} \quad (15)$$

where K_0 is the background diffusivity; Ri is the gradient Richardson number, defined as $Ri = -\frac{g}{\rho_w} \frac{\partial \rho / \partial z}{(\partial u / \partial z)^2}$; and ρ_w is the water density, which is dependent on the water pressure, salinity, temperature, and sediment concentration.

In the model simulation, one cohesive sediment type was specified in the FVCOM sediment module with a median grain size of 0.008 mm, sediment density (ρ_s) of 2650 kg/m³, porosity of 0.5, and default settling velocity ($w_{s,0}$) of 0.4 mm/s. These parameters were adopted from Ge et al. (2015). Assuming an insignificant morphological evolution over a short-term simulation under calm weather conditions, we set the seabed morphology as a constant during the model run.

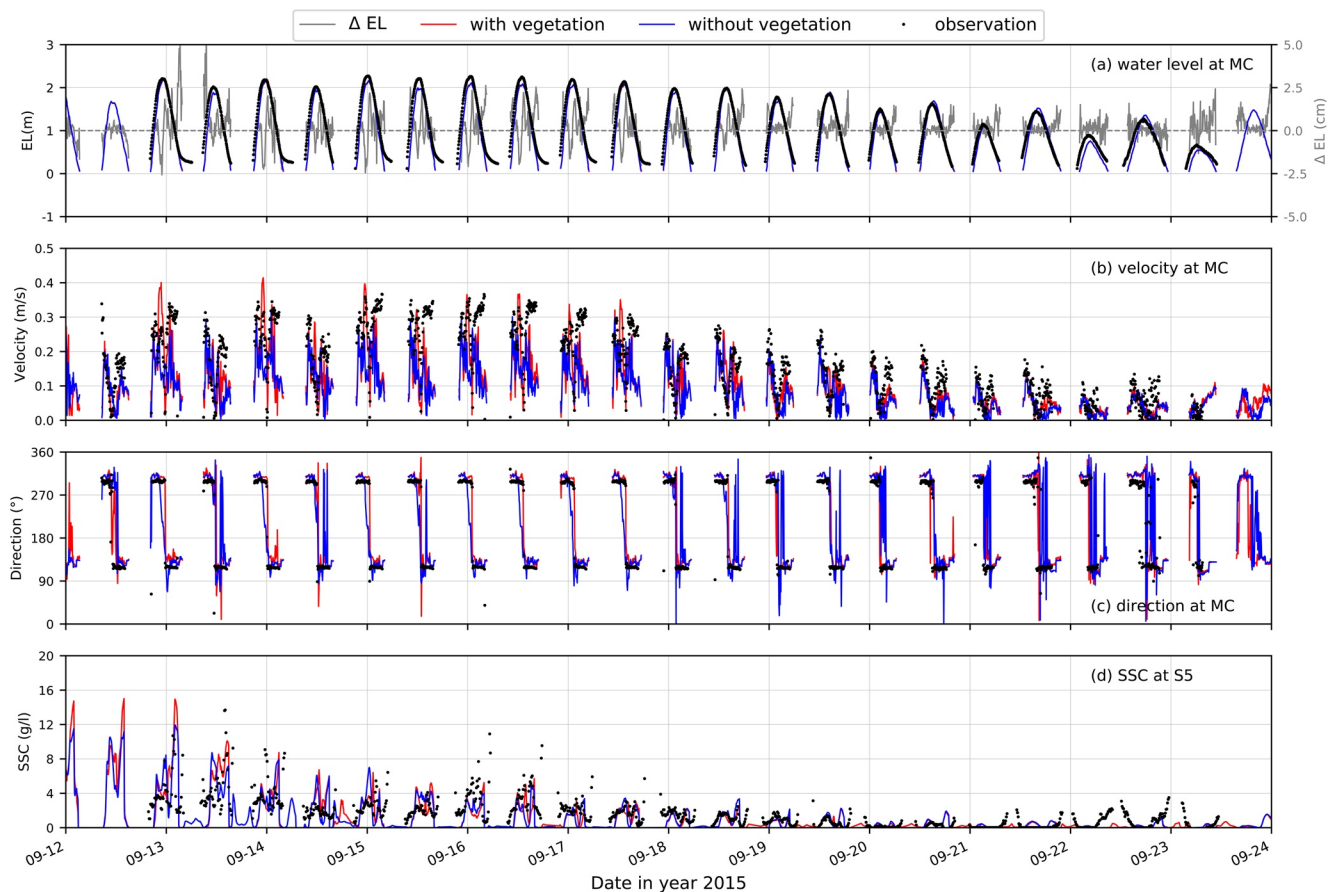


Figure 5. Model-data comparisons. (a) Tidal elevation, (b) flow speed, (c) flow direction, and (d) suspended sediment concentration. The red and blue curves indicate the vegetated and nonvegetated results, respectively. The gray curve in (a) shows the difference between vegetated and nonvegetated cases. Flow directions of approximately 300° and 120° suggest flood and ebb currents, respectively.

3. Results

3.1. Model Validation

The coupled model system ran from September 1 to 25, 2015, covering the observational period at site MC. The vegetated and nonvegetated models were validated by comparing the simulated water elevations and velocities with observed data (Figure 5). The results show that the vegetation-coupled model was robust in reproducing observed water levels and currents, not only over a short duration but also at the rapid transitions between flood and ebb tidal periods (Figure 5). When the tidal currents turned to a flood phase at site MC, the velocity rapidly increased to a maximum of 0.4 m/s. Afterward, the flow abruptly changed to an ebb tidal stage (Figure 5c). Both the observed and simulated velocities contained noticeable high-frequency oscillations during the ebb tidal period, suggesting the influence of water confluence from adjacent salt marshes on the flows in the tidal creeks (Figure 5b). Successful current and water level simulations produced reasonable sediment variations at site S5, a nearby salt marsh location. The model captured the amplitude and variation patterns of SSC over the spring-to-neap cycle. During spring tidal cycles, the SSC reached ~ 14 g/L (Figure 5d).

Three statistical error methods were used to assess the model performance for the cases with and without vegetation, including the root mean square error (RMSE), Willmott skill score (WS), and correlation coefficient (CC) calculated by using Willmott's (1981) algorithm. The expressions of these three methods are given as follows:

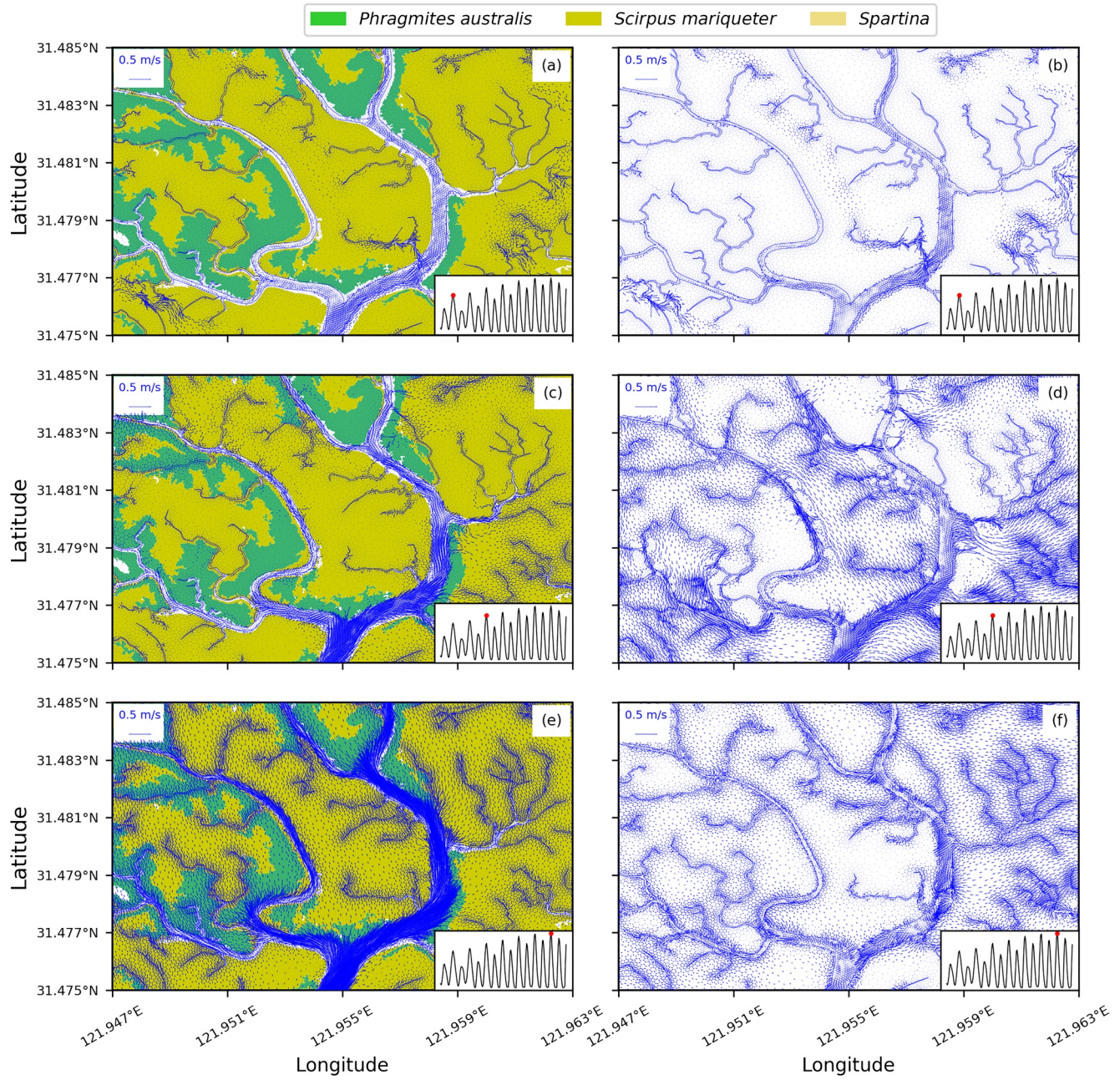


Figure 6. Enlarged view of the near-surface flow around the middle creek during the flood tidal period over a neap-to-spring tidal cycle in the vegetated (left column) and nonvegetated (right column) cases. The shaded polygons indicate the coverages of various vegetation types.

$$RMSE = \sqrt{\sum_{i=1}^N (X_m - X_o)^2 / N} \quad (16)$$

$$WS = 1 - \frac{(X_m - X_o)^2}{\left(|X_m - \bar{X}_o| + |X_o - \bar{X}_o| \right)^2} \quad (17)$$

Table 2

Error Statistics Including the Root Mean Square Error (RMSE), Willmott Skill Score (WS), and Correlation Coefficient (CC) of the Modeled Water Level, Flow Velocity, Direction, and SSC With/Without Vegetation

	Water level (m)		Velocity (m/s)		Direction (°)		SSC (g/L)	
	Veg	No-veg	Veg	No-veg	Veg	No-veg	Veg	No-veg
RMSE	0.18	0.18	0.094	0.108	17.4	14.2	1.91	2.30
WS	0.97	0.97	0.74	0.61	0.97	0.94	0.58	0.44
CC	0.67	0.67	0.62	0.54	0.92	0.85	0.45	0.39

$$CC = \frac{\sum_{i=1}^N (X_m - \overline{X_m})(X_o - \overline{X_o})}{\left[\sum_{i=1}^N (X_m - \overline{X_m})^2 \sum_{i=1}^N (X_o - \overline{X_o})^2 \right]^{1/2}} \quad (18)$$

where X_m and X_o indicate the observed and modeled values, respectively.

The statistics regarding the modeled errors in water elevation, flow velocity and direction, and SSC for the cases with and without vegetation, are shown in Table 2. The RMSEs were 10.8 and 9.4 cm/s in speed, 17.4° and 14.2° in direction, and 2.3 and 1.9 g/L in SSC for the cases without and with vegetation, respectively. This demonstrates that the model with vegetation provided better simulations of flows and SSC than the model without vegetation. Vegetation did not influence the water levels in

low-elevation tidal creeks since the results from the two cases were identical in these areas. The simulated water elevation was higher in the vegetated case than in the nonvegetated case (gray curves in Figure 5a), especially during the early flood and late ebb tidal periods. The nonvegetated model significantly underestimated the flood peaks and durations (Figures 5b and 5c), even though the RMSEs for the two cases were close to each other. This underestimation was due to an overestimation of the water transport onto the salt marsh in the nonvegetated cases. During the spring tidal cycles, the maximum difference between the two instances reached ~10 cm/s or greater in velocity and ~50% in flood duration. Since the sediment transport was mainly controlled by the flow intensity and direction, it also showed a significant difference between the two cases.

3.2. Flows

The surface flow distribution around Chongming Dongtan during the flood and ebb tidal periods is given in Supporting Information S2–S3. To examine the differences in the change in flow from the neap-to-spring tidal cycle for the cases with and without vegetation, we selected a subarea where the tidal creek split into eastern and western branches and was surrounded by abundant vegetation (Figure 6). At high tide during the neap cycle, the flows of the two cases displayed similar spatial distributions (Figures 6a and 6b). The flow was much weaker in the salt marsh at the high tide of the transitional cycle in the vegetated case (Figures 6c and 6d). As a result, the velocity in the tidal creek was stronger under vegetated conditions than under nonvegetated conditions. In turn, the lateral currents in the salt marsh were much stronger under the nonvegetated condition than in the vegetated case during the transition stage (Figures 6c and 6d). It is clear that vegetation significantly suppressed lateral flow in the salt marsh, even though it did not change the flooding process between tidal creeks and salt marsh. These features remained at high tide during the spring tidal cycle (Figures 6e and 6f). A much stronger flow was found in the tidal creek in the vegetated case than in the nonvegetated case. Moreover, the flow direction in the salt marsh differed between the two cases, showing northward behavior under the vegetated case and westward behavior under the non-vegetated case.

At low tide during the spring tidal cycles, most regions of Chongming Dongtan underwent draining processes (Supporting Information S3). However, some scattered areas were fully covered by water due to the presence of low-lying mudflats surrounded by vegetation. The velocities in these scattered residual waters were generally minimal, except at some spots where the flows into nearby small creeks reached 10–20 cm/s. The water in the creeks and within the vegetated salt marsh flowed in the same direction during the ebb tidal phase. *P. australis* grew in relatively higher-elevation salt marsh areas, where no residual water existed at low tide. *S. alterniflora* covered the deeper regions where water remained at low tide.

We compared flows over tidal cycles at site A (a low tidal flat) and site B (a high tidal flat) (Figure 2b). The tidal flows were strongly affected by vegetation in both the high and low tidal flats (Figure 7). The presence of vegetation changed not only the flow magnitude but also the flow direction. During the spring tidal cycle, site A experienced an intense flooding/draining process. The water only covered this site at high tide (Figure 7b). Vegetation significantly weakened the tidal flow and caused the flow direction to change by

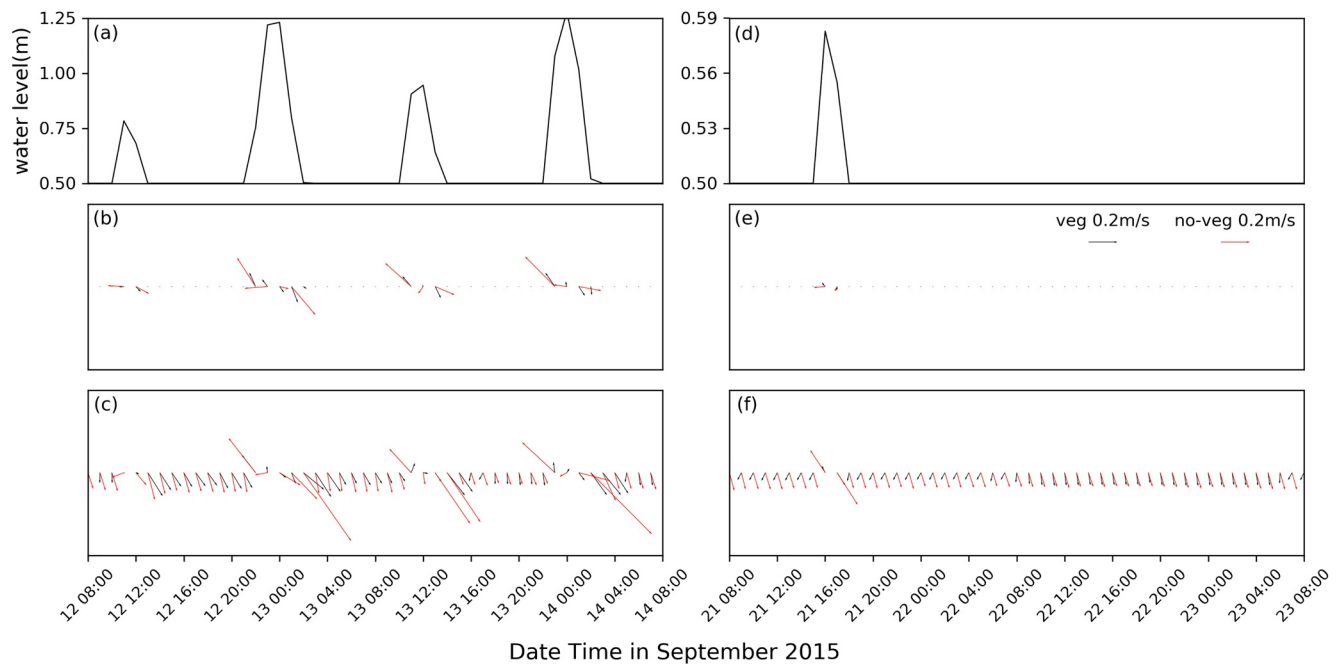


Figure 7. Time series of water level (upper row) and surface flow vectors at site A in a low tidal flat (middle row) and at site B in a high tidal flat (bottom row) during the spring (left column) and neap (right column) tidal cycles. The locations of sites A and B are shown in Figure 2b. The black and red vectors indicate tidal flows under the vegetated and nonvegetated cases, respectively.

~50° and even up to ~70° during the weak-flow period of ebb tide. During the neap tidal cycle, site A dried out (Figure 7e).

A persistent weak tidal flow dominated site B during the tidal cycles (Figures 7c and 7f). The flow was generally less than 0.2 m/s, except at high tide. The velocity was ~50% weaker in the vegetated case. Similar to site A, vegetation also caused a significant change in flow direction. The flow comparison results in high and low tidal flats suggest that vegetation influences not only the flow magnitude but also flow direction. Ignoring vegetation may cause a significant bias in the model-produced transport of dissolved and particulate matter.

3.3. Salinity

Around the outer sea region, the salinity was ~10–15 PSU (Figure 8a). The high-elevation areas near dikes and in the salt marsh had salinities of ~15–18 PSU, while major creeks and adjacent regions had lower salinities of ~4–10 PSU. These low-salinity waters originated from riverine water that had flowed first to the outer sea during the previous ebb tidal period. Then, an onshore flow pushed the water into the tidal creeks and low-elevation mudflats during the flood tidal period. Relatively fast upstream transport occurred along the tidal creeks, carrying the low-salinity water further to the north, and lateral transport occurred from tidal creeks to the nearby salt marsh. Comparatively, the vegetated salt marsh areas far away from major creeks were mainly dominated by high-salinity water.

Without vegetation, the flows in the salt marsh and edges of tidal creeks were overestimated. The salinity difference was much smaller between tidal creeks and the nearby salt marsh in the nonvegetated case. During the high-tide period, relatively uniform low-salinity water was everywhere, from the low-to high-elevation salt marsh (Figure 8b).

The time-averaged salinity distributions in the spring cycle showed relatively higher salinity values (~5 PSU) in the vegetated salt marsh areas and lower salinity values (1–2 PSU) in the creeks (Figure S5a). Since water flooding strongly decreased during the neap cycle, only the low-elevation salt marsh areas were influ-

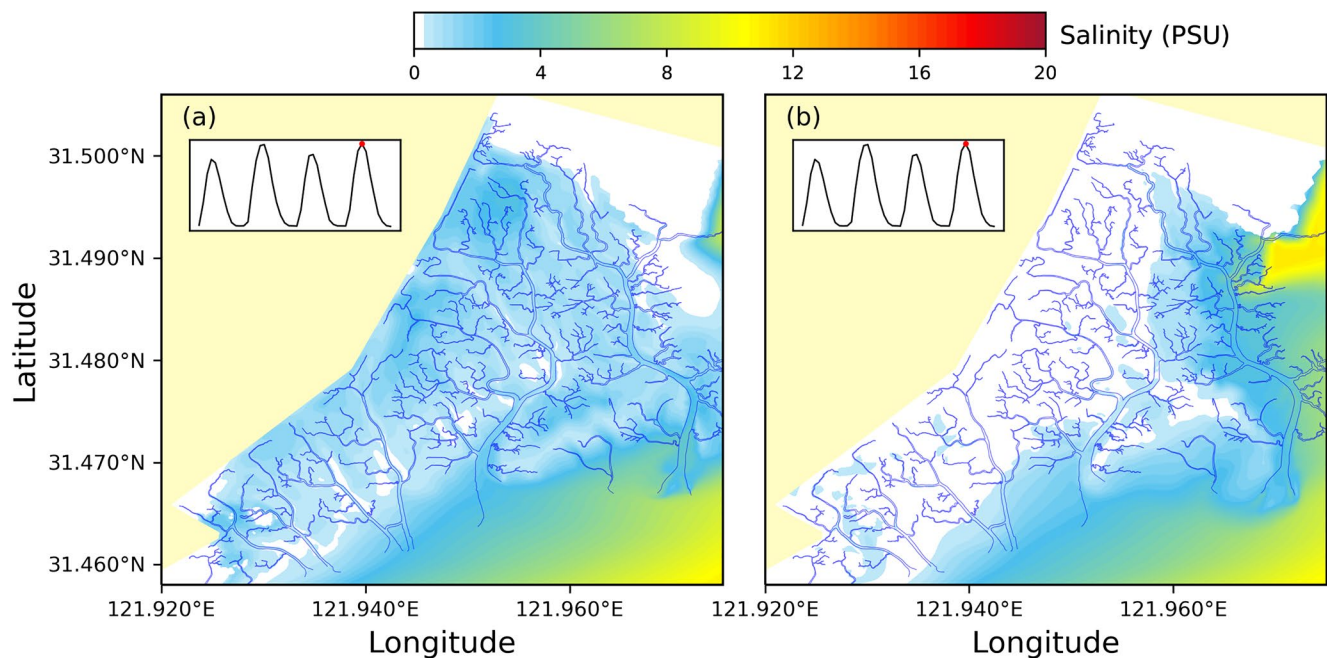


Figure 8. Surface salinity in Chongming Dongtan at high tide during a spring tidal cycle for cases with (a) and without (b) vegetation.

enced by tidal fluctuations in this phase. However, the mean salinity (>5 PSU) averaged over a neap tidal cycle was relatively higher than that averaged over the spring cycle (Figure S5b).

3.4. Suspended Sediments

The flooding and draining processes resulted in significant variations in suspended sediments (Figure 9). Most Chongming Dongtan areas were occupied by water during the flood tidal period (Figure 9a). At high tide, high suspended sediment concentrations (SSCs) appeared mainly in regions around tidal creeks and deep waters. In these regions, the SSCs reached 10 g/L or higher (Figure 9a). Since the simulated wave energy was weak due to vegetation-induced attenuation over the salt marsh (see Supporting Information S4), these high SSCs were primarily caused by strong tidal flows along tidal creeks. These flows advected waters from the creeks into the salt marsh during the flood tidal period. The SSCs remained low over vegetated salt marsh disconnected from major creeks, suggesting that weak flows and turbulence in the vegetated patches favored sediment deposition but not erosion or resuspension.

At low tide during the spring tidal cycle, noticeable SSCs (>6 g/L) appeared only in several major creeks (Figure 9b). The resident flows in the salt marsh were too weak to provide adequate turbulent kinetic energy for sediment suspension. This was the reason why the SSCs were low in the mudflats and vegetated salt marsh. During the ebb tidal period, several tidal creeks remained in wet conditions. The remaining water in these creeks was sourced from the adjacent salt marsh. As a result, these tidal creeks had relatively higher SSCs (~ 2 g/L or less). The maximum concentration reached ~ 8 g/L, occurring in the middle creek.

In the salt marsh, high SSC values occurred mainly within tidal creeks and adjacent estuarine regions. The SSC variation was primarily affected by tidal currents and waves in the tidal creeks. The simulated results demonstrate that the tidal flow was much stronger under vegetated conditions than under nonvegetated conditions (Figure 5). This explains why the SSCs around tidal creeks in the southwestern area were higher under vegetated conditions than under nonvegetated conditions (Figure 9a). These high-SSC waters were transported to the nearby region during the high-water-level period. On the other hand, under nonvegetated conditions, since the water is free to flush or drain out of the salt marsh without resistance from vegetation-induced drag, a more substantial tidal flow can appear in the northern area near the dike. As a result, an unrealistically high SSC patch could occur in that area (Figure 9b).

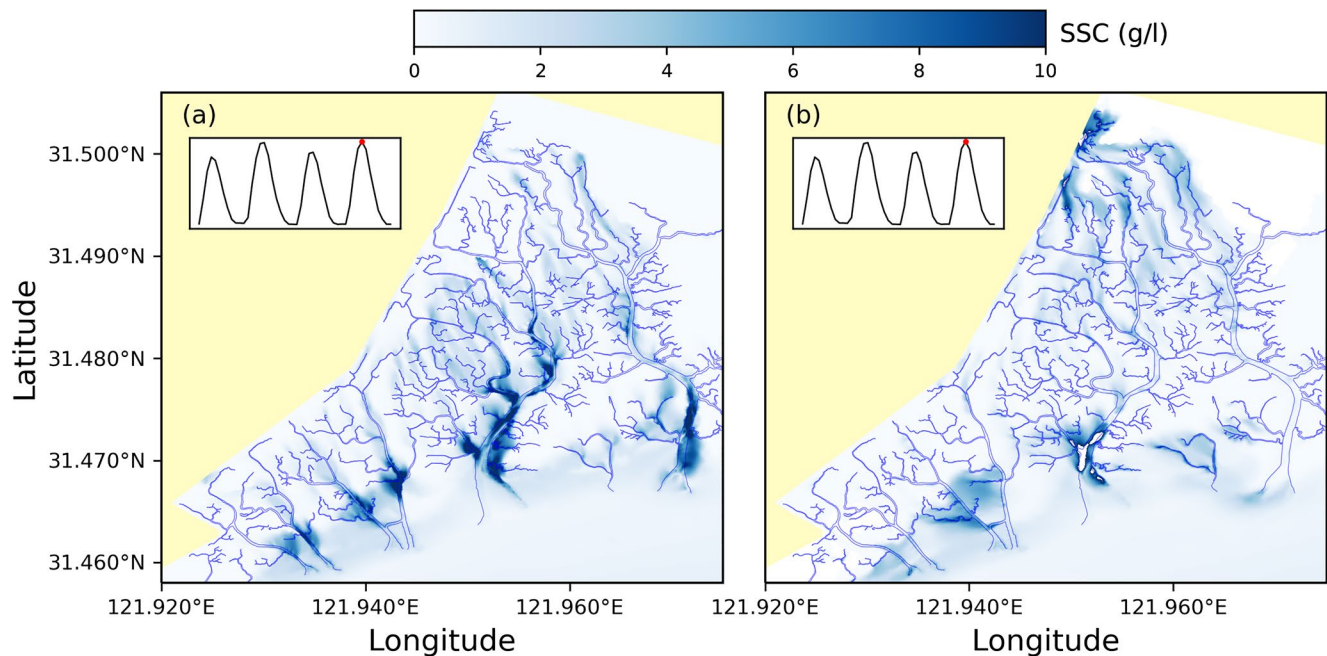


Figure 9. Suspended sediment concentration in Chongming Dongtan at high tide during a spring tidal cycle for cases with (a) and without (b) vegetation.

3.5. Lateral Exchanges

We selected the largest tidal creek in the middle of Chongming Dongtan to examine the impact of vegetation on lateral transport (see the location in Figure 2a). This tidal creek featured mixed coverage of *P. australis* and *S. alterniflora* (Figure 2b). The influx and outflux were calculated by measuring the water transports through boundaries, including in Section 3 at an outlet and in Sections 1 and 2 for the lateral edges (Figure 2a).

The time series of water and sediment fluxes at the salt marsh outlet over a period from September 10 to 24 are shown in Figure 10. The water flux mainly followed tidal variation, with positive onshore peaks during the flood tidal period and negative offshore peaks during the ebb tidal period. During a neap tidal cycle, the water flux was almost negative, providing net offshore water transport from tidal creeks to the sea. The maximum value of this transport was $\sim 55 \text{ m}^3/\text{s}$. During the spring tidal cycle, significant residual waters remained in the salt marsh after the ebb tidal period (Figure 8b). These waters gradually flowed into the peripheries and finally entered the creek in the subsequent neap tidal cycle. This process produced net offshore transport with a daily mean flux of $\sim 31 \text{ m}^3/\text{s}$. The transport varied significantly with tidal variations. The maximum flux was $298 \text{ m}^3/\text{s}$ during the flood tidal period and $-340 \text{ m}^3/\text{s}$ during the ebb tidal period. These results demonstrate that the tidal creek functioned as a water pathway for water exports from the salt marsh to the offshore region.

As described above, a vegetated salt marsh can enhance tidal flows in tidal creeks (Figure 5b), especially around low-elevation regions. These intensified flows produce much larger water and sediment fluxes during the spring tidal cycle and spring-neap tidal transition. These fluxes were significantly lower in the case without vegetation. In this case, the maximum onshore and offshore water fluxes were 198 and $-143 \text{ m}^3/\text{s}$, respectively (Figure 10b), $\sim 33.6\%$ and 57.9% lower than the fluxes obtained in the case with vegetation.

Similarly, the maximum onshore and offshore sediment flux rates were 3,249 and $-4,785 \text{ kg/s}$ for the case with vegetation and 2,136 and $-1,127 \text{ kg/s}$ for the case without vegetation, respectively. Ignoring vegetation caused the underestimation of the onshore and offshore sediment flux rates by 34.3% and 76.4%, respectively. At the outlet, the sediment flux was strongly related to the water flux, with average values of -145 kg/s during the spring tidal cycle and -1.23 kg/s during the neap tidal cycle. The maximum positive and nega-

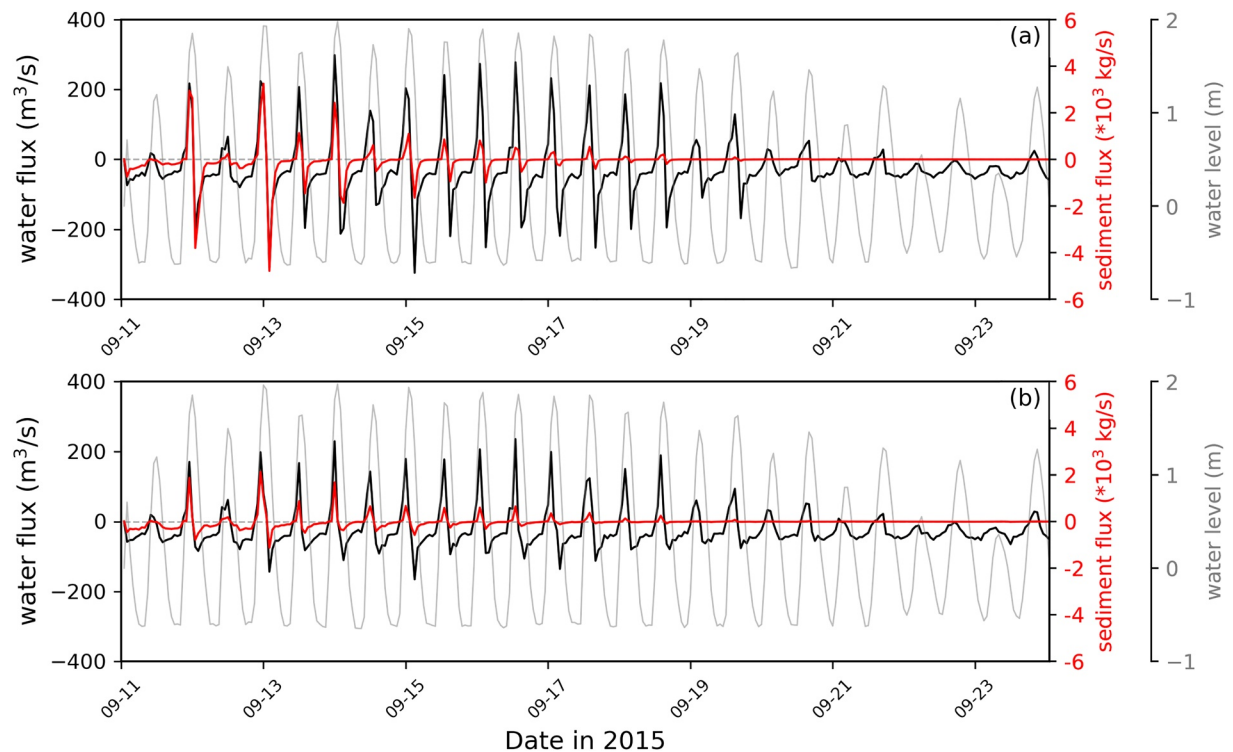


Figure 10. Time series of tidal elevations (light gray), water fluxes (black), and sediment flux (red) rates through the outlet transection of the middle creek (September 11–25, 2015). Results are shown for cases (a) with and (b) without vegetation. The positive and negative values indicate onshore and offshore fluxes, respectively.

tive fluxes reached 3,249 and $-4,785$ kg/s over the flood and ebb tidal periods during the spring tidal cycle, respectively. The fact that the net contribution through the outlet was not zero during the selected period suggests that the water transport in tidal creeks did not reach a state of equilibrium, nor did the lateral transport on either side of the tidal creeks.

The flux rate per unit length was calculated along the two nearby lateral boundaries in the selected tidal creek (Figure 11). This rate significantly varied along these lateral edges. The rate was higher at the low-elevation creek outlet than at the high-elevation salt marsh area. During the neap tidal cycle, the tidal creek did not show significant lateral water fluxes (Figure 11b). During the flood tidal period, the two lateral boundaries experienced different flux directions (Figures 11b and 11c). On the western edge, the low-elevation portion (Section 1) exhibited an outflowing flux, while the high-elevation area experienced a weak inflowing flux (Figure 11b). The mid-elevation segment between the high- and low-elevation areas acted as a transition zone. During the ebb tidal period, the in-creek lateral flux was dominant.

The eastern boundary (Section 2) showed an opposite trend to that of the western boundary during the flood and ebb tidal periods (Figure 11c). During the flood tidal period, the low- and high-elevation segments featured in-creek and out-creek fluxes, respectively. During the ebb tidal period, the out-creek flux was weak in the low-elevation segment. At low tide, the low-elevation element was characterized by an in-creek flux. The maximum flux rate per unit length was ~ 0.18 m²/s.

The sediment fluxes along these eastern and western boundaries are shown in Figure 12. The fluxes were significant during the spring tidal cycle and spring-neap transition and negligible during the neap tidal cycle. On the western boundary, the sediment flux was negative during the flood tide period and positive during the ebb tidal period (Figure 12b). Correspondingly, the sediment flux was oriented in the same direction as the water flux (Figure 11), with a maximum value of 1.5 kg / m · s. On the eastern boundary, the sediment flux variation was opposite to that on the western boundary (Figure 12c). Both lateral boundaries showed significant sediment fluxes in low-elevation regions. For the mid- and high-elevation areas, the sediment fluxes were very weak due to low SSCs in these areas (Figure 9a).

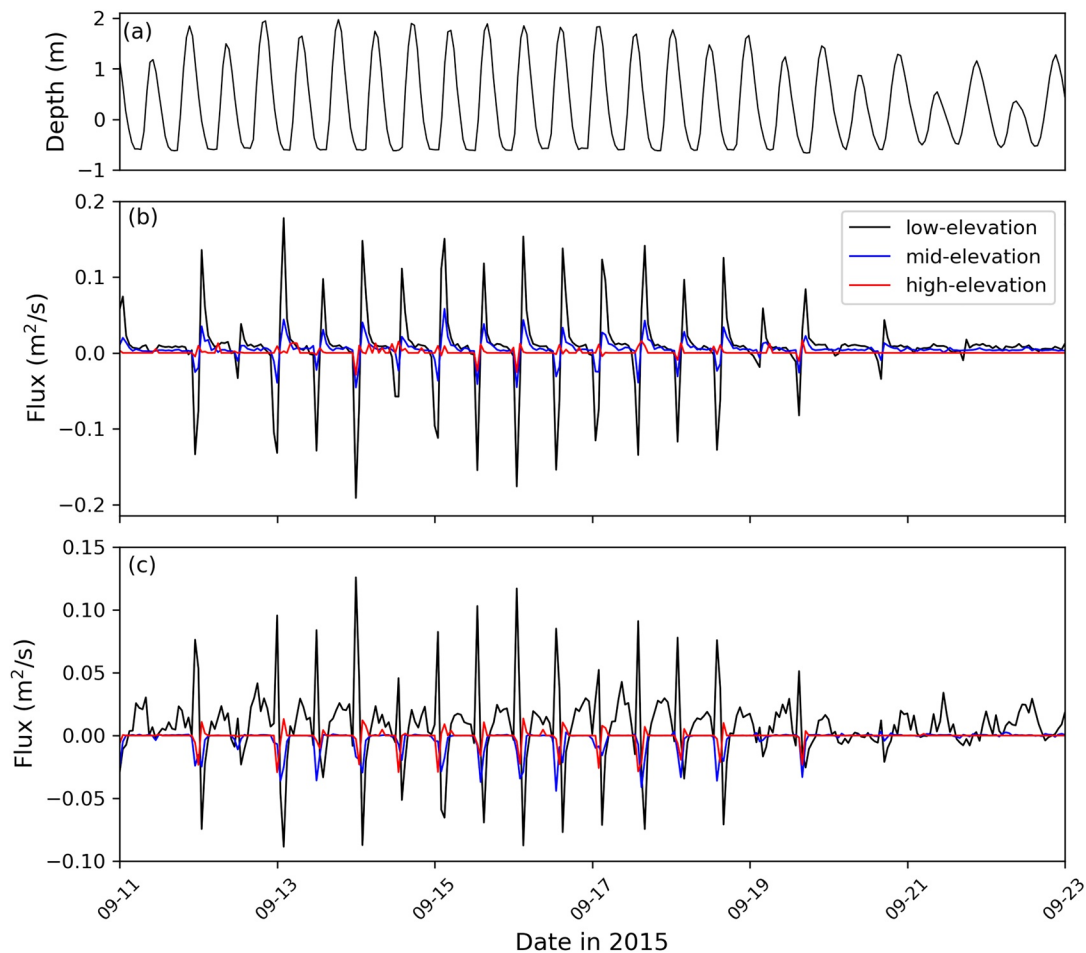


Figure 11. Changes in tidal elevations and water fluxes with time. Time series of the (a) tidal elevation and water flux rate through the (b) west and (c) east boundaries along the middle creek. The positive and negative values indicate fluxes into and out of the creek. The black, blue, and red curves indicate the averaged flux rates in the low-, mid-, and high-elevation lateral boundaries.

3.6. Lagrangian Flows

In a tidal-dominant, estuarine-tidal creek-salt marsh complex, water and sediment are carried by Lagrangian residual flows (Chen et al., 2008). One hundred particles were randomly released at the sea surface in a circular area with a radius of 500 m, centered at 121.955°E and 31.46°N, at the beginning of the flood tide at 20:00 GMT on September 12, 2015. The tracking time was set to four hours in the flood tidal period. The particle trajectories displayed multiple flow paths. Some particles first moved westward along mudflats, turned landward to enter the middle area of the salt marsh, and then flowed into the offshore area (Figure 13a). Most particles were pushed into the middle area of the tidal creek. These particles moved rapidly upstream along the creek, and some particles entered the western salt marsh. The particle movements were consistent with the out-creek lateral flux determined in the low-elevation segment of the western boundary (Figure 11b). From the same release area, several particles moved much further than others, crossing the western creek boundary to reach the adjacent salt marsh. These results suggest that the tidal creek was not a final destination for water.

We also released particles randomly in a circle of the same size located in the high-elevation salt marsh area at 00:00 GMT on September 13, 2015 and tracked the particles for 6 hours during the ebb tidal period (Figure 13b). Many of these particles moved in parallel in the same direction, but most remained in the salt marsh. These results suggest that these particles were stranded when the land was either emergent or submerged by residual waters. Some particles first entered tidal creeks and then joined together to move into the deep offshore region.

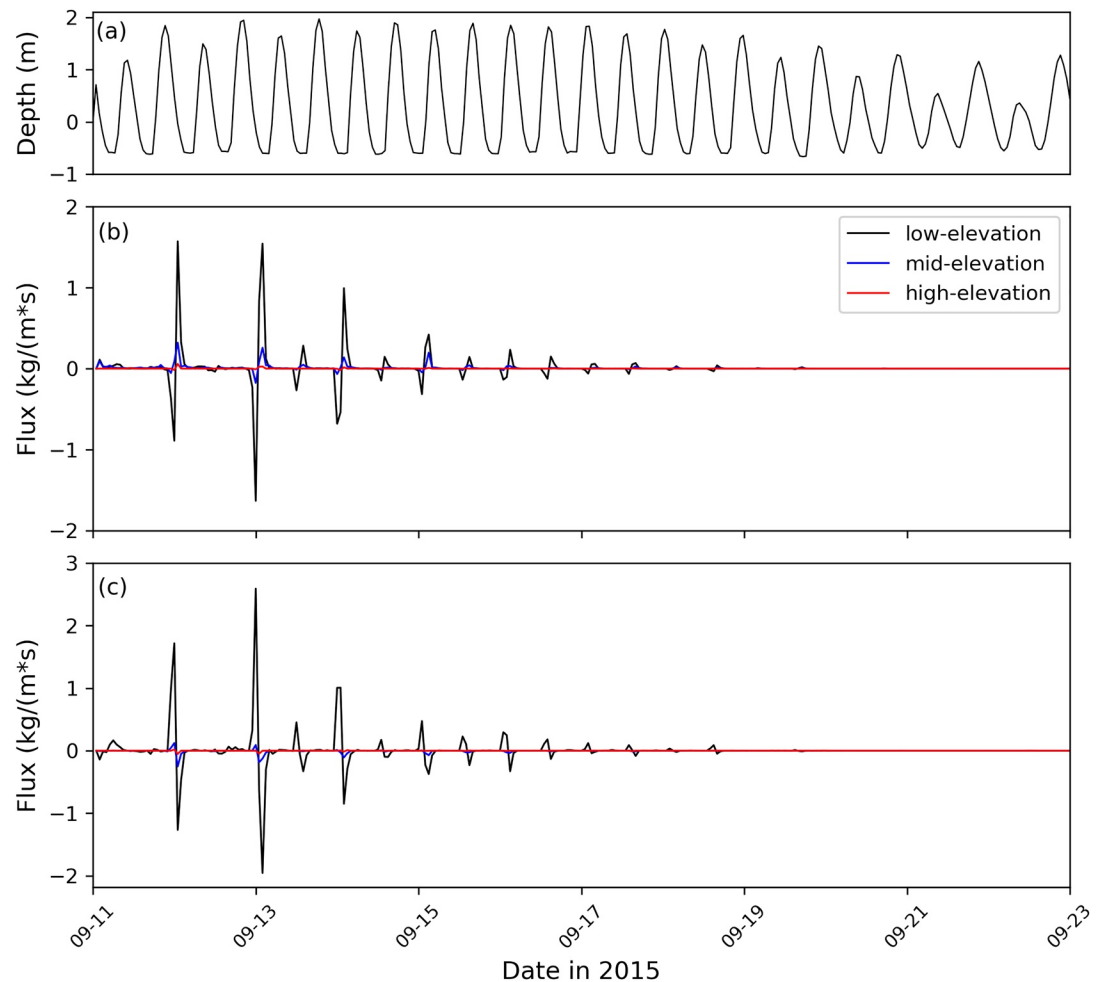


Figure 12. Tidal elevations and sediment fluxes with time. Time series of (a) tidal elevations and sediment fluxes through the (b) west and (c) east boundaries along the middle creek. The positive and negative values indicate fluxes into and out of the creek, respectively. The black, blue, and red curves indicate the averaged flux rates in the low-, mid-, and high-elevation lateral boundaries.

4. Discussion

4.1. Salinity Implications on Halophytic Vegetation

Although *P. australis*, *S. mariqueter*, and *S. alterniflora* are all halophytic vegetation types that are present in the studied salt marsh, they have different salt and flooding tolerances that control their growth and distribution (Ge et al., 2014; Gulzar et al., 2007; Vélez-Martín et al., 2020). The interactions among freshwater discharge, oceanic saltwater, and tidal currents can result in substantial salinity variations in the salt marsh, even under high river flow conditions during summer.

The vegetated simulation case predicts the salinity distribution over the neap-to-spring tidal cycle and at the tidal transition stage (Figure 14). In this simulation, the salinity in the low-elevation mudflat remains relatively high (~6–8 PSU) during the neap tidal cycle, including during the neap-to-spring tidal transition stage (Figures 14a and 14b), and then becomes low during the spring tidal cycle (Figures 14c and 14d). This temporal variation with the tides agrees well with previous salinity observations obtained in the Changjiang River Estuary (Ge et al., 2018; Zhou et al., 2019). Weak tidal mixing in the low-energy neap cycle leads to a large landward baroclinic pressure gradient force and thus causes saltwater intrusion. Moreover, the model predicts low-salinity water coverage in the high-elevation salt marsh area where *P. australis* dominates and high salinity in the low-elevation salt marsh region where *S. alterniflora* is the primary plant type. Physio-

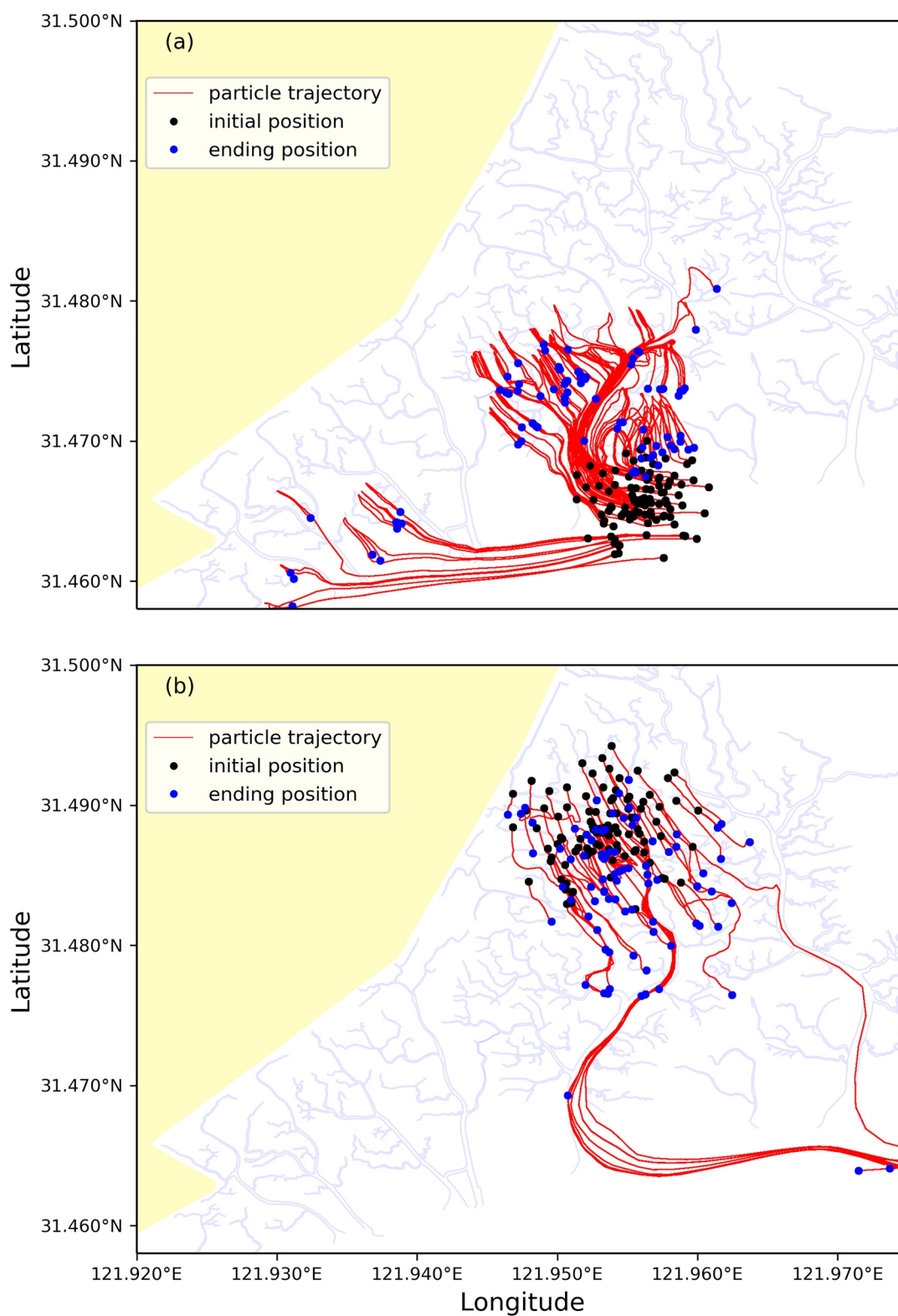


Figure 13. Lagrangian particle trajectories of 100 random surface particles. (a) Particles released in the low-elevation mudflat at 20:00 GMT on September 12, 2015 and tracked for four hours during a flood tide period; and (b) particles released in the high-elevation salt marsh at 00:00 GMT on September 13, 2015 and tracked for six hours during an ebb tide period. The black and blue dots indicate the initial and ending particle positions, respectively.

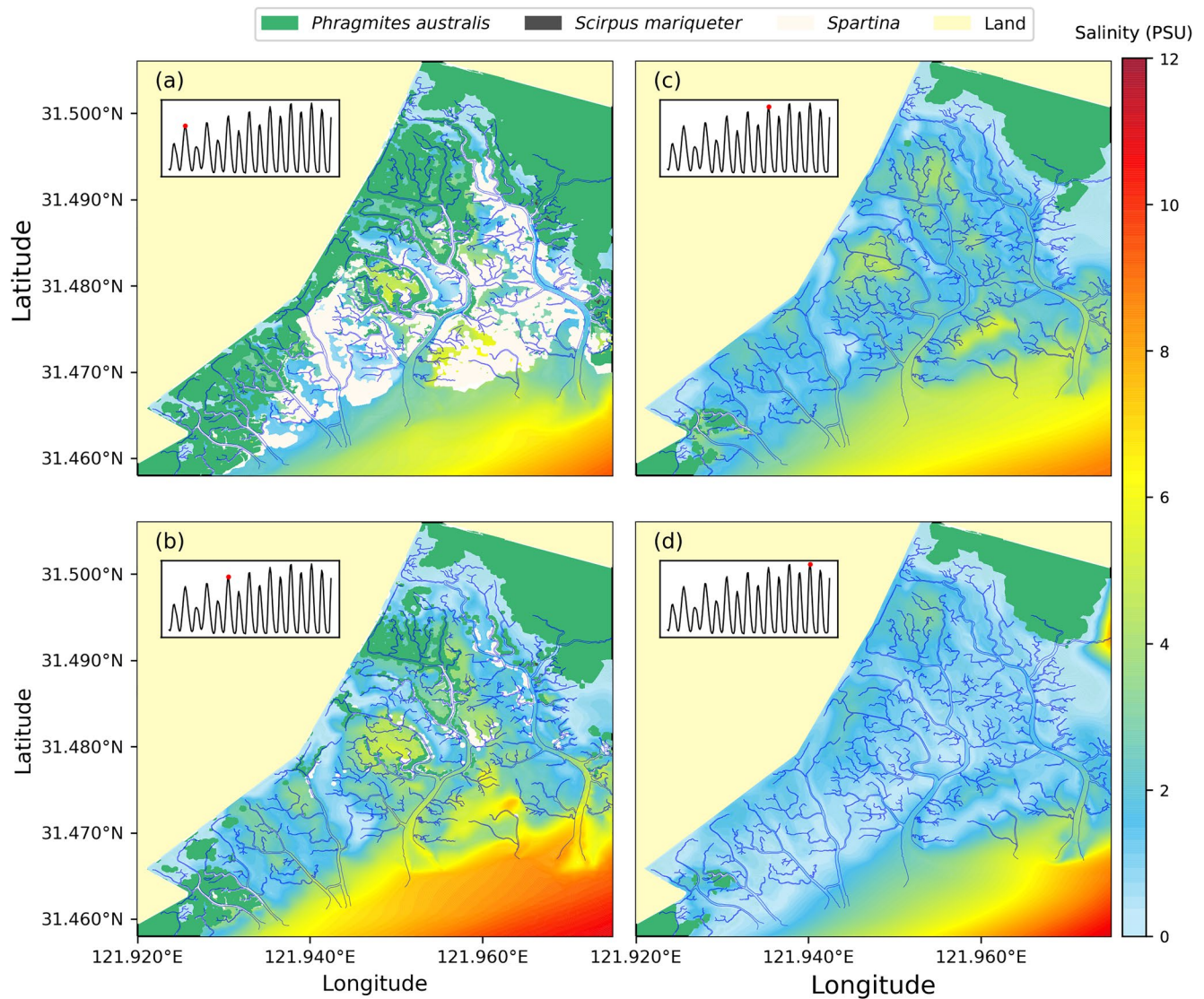


Figure 14. Salinity distributions at high tide during the neap (a), pretransition (b), transitional (c), and spring (d) tide periods. The vegetation information is overlain.

logical experiments indicate that *S. alterniflora* can grow under conditions within the salinity range of 3–15 PSU, showing better salt tolerance than *P. australis* (Ge et al., 2014; S.-H. Li et al., 2018). Below this salinity level, the *S. alterniflora* biomass significantly decreased.

S. alterniflora has a parabolic response to flooding: too little or too much flooding reduces productivity (Morris et al., 2002). Optimal flooding levels can have a positive effect on grass growth and biomass. Waterlogging results in grass dieback, as it leads to a buildup of porewater sulfides that are toxic to roots. Therefore, waterlogging can control the growth and spread of *S. alterniflora* in the salt marsh (Yuan et al., 2011). During spring tide, the low-elevation region experienced a longer flooding duration, lasting ~6–7 h (Supporting Information S5). However, the flooding duration in the high-elevation salt marsh was ~2–3 h. During the neap cycle, the flooding duration in the high-elevation region dramatically decreased, lasting only ~1.2 h or less. In contrast, the flooding duration in the low-elevation area significantly increased, lasting ~8 h (Supporting Information S5). The salt marsh with longer flooding durations experienced higher salinity. Waterlogging often causes grass dieback and the formation of mudflats or ponds (Zhang et al., 2019). However, moderate rates of SLR can have positive effects on *S. alterniflora* growth and expansion of the current spatial extent. The relationship between salinity and vegetation zonation implies that climate change-induced

SLR tends to increase saltwater intrusions and reshape vegetation species distributions in salt marshes (S.-H. Li et al., 2018; Wiberg et al., 2020). This information is essential for salt marsh management and may be linkable to expansion of the spatial extent of *S. alterniflora*.

In the estuarine-tidal creek-salt marsh complexes, both hydrodynamics and morphodynamics vary with vegetation. Yuan et al. (2014) found that the three major vegetation species did not show any dominance in the past regarding their spatial coverage in Chongming Dongtan. The vegetation in the salt marsh experienced substantial spatiotemporal variabilities on scales from seasons to decades. To estimate the impact of this variability on hydrodynamics, an additional experiment was conducted. This experiment was configured with the observed vegetation distribution in the summer of 2017 (hereafter referred to as the 2017-veg case) and ran in the same complex region (Supporting Information S6) under the same tidal, atmospheric, and river boundary forcings as those used in the September 2015 simulation (hereafter referred to as the 2015-veg case). In this experiment, the same interpretation method was used to determine the vegetation patches from the multispectral Pleiades remote sensing data. Comparing the two cases between 2015 and 2017 vegetation allowed us to examine how hydrodynamics varied with vegetation.

Salinity was chosen to represent the hydrodynamics around Chongming Dongtan. By changing the baroclinic density gradients, salinity can affect water flows and transport. The difference in salinity between the 2015-veg and 2017-veg cases at high tide is shown in Supporting Information S7. The results indicate that when the salt marsh and tidal creeks are mostly submerged, the presence of different vegetation types could cause a significant change in the salinity distribution. This change was associated with the random shifting of vegetation, which is distributed nonuniformly in space. The maximum salinity variation range was over ± 4 PSU. This suggests that rapidly evolving vegetation in the salt marsh can significantly modify local and regional hydrodynamics. These changes in salinity and sediment transport can consequently affect geomorphology. In turn, since hydrodynamic features and vegetation are closely related, spatiotemporal variations in flow and salinity could potentially impact vegetation growth and migration.

Furthermore, the biomechanical properties of vegetation, such as vegetation height, elasticity, and diameter, vary throughout the life cycles of plants, and these variations can produce significantly different impacts on flows, waves, sediments, etc., (Zhu et al., 2019). In our simulations, the flexible blade height (l_v) was assumed to be constant. This constant was chosen to be a mean value averaged over the summer season, as obtained from a vegetation survey. This assumption is reasonable for a simulation with a fortnight time scale since vegetation growth is insignificant over this short period. However, when a long-term simulation, for example, over a seasonal to annual scale, is conducted, we must consider the spatiotemporal variability in l_v . More extensive surveys are required to cover the spatial distributions of stem heights for various vegetation species and to produce a spatially nonuniform l_v value. Taking a varying l_v into account could help us better resolve the influence of vegetation on lateral tidal flows.

4.2. Sediment Import and Export

Salt marshes frequently experience rapid evolution, expanding or eroding over several hundred-meter scales over a few years, especially along their lateral extents (Fagherazzi et al., 2013; Leonardi et al., 2016; X. Li, Plater, & Leonardi, 2018; Li et al., 2019; Yang et al., 2001). One of the dynamic causes of this evolution is sediment imports and exports under different physical conditions around salt marshes. Long-term and large-scale surveys have revealed that sediment supplies dominated the expansion of salt marshes in northern England and erosion in southern England (Ladd et al., 2019). The Changjiang River Estuary provides an abundant sediment supply, not only for Chongming Dongtan but also for most salt marshes distributed in the estuary and adjacent regions, such as the Jiuduansha Shoal and Nanhui Shoal (Yang et al., 2019). Vegetation in a salt marsh modifies the flow patterns over tidal cycles, reducing erosion, attenuating storm surges and waves, and mitigating sea-level rise through sedimentation (Temmerman et al., 2012). Our simulation results suggest that suspended sediment is scarcely transported farther into the vegetated salt marsh during the flood tidal period due to the associated flow reductions, increased settling, and limited water depths (Figure 9a). This feature was also observed in a marsh-dominated estuary, Plum Island Sound, on the Massachusetts coast, USA (Zhang et al., 2019). In a vegetated salt marsh, the fast and enhanced erosion resulting from extreme weather events, e.g., tropical cyclones or storms, could be rapidly recovered with a

high accretion rate under stable hydrodynamic conditions (Temmerman et al., 2005; Xie et al., 2017). Moreover, most sediments deposit in mudflats, vegetation edges, and tidal channels, result in lateral extension.

More specifically, sediment imports and exports within tidal creeks are critical factors determining the growth or degradation of creek networks. In this study, a negative (seaward) suspended sediment flux was identified during the tidal cycle. A similar pattern was also found in tidal creeks in northern San Francisco Bay, even during a storm surge (Lacy et al., 2018). Positive (landward) sediment fluxes mainly occur under wave-dominated suspension and moderate tidal conditions, producing greater-than-average SSC values during the flood tidal period (Green & Hancock, 2012; Lacy et al., 2018; X. Li, Plater, & Leonardi, 2018; Li et al., 2019). Sediment imports and exports also vary significantly with season (Poirier et al., 2017).

It should also be pointed out that our model outcomes differed from the results shown in S.-H. Li et al. (2018), Li et al. (2019). The possible reason for this was due to the different spatial scales and forcings used in the different studies. S.-H. Li et al. (2018), Li et al. (2019) considered a large-scale salt marsh, while our focus was on local tidal creeks. They considered waves and macrotides as the primary forcings, while we took river runoff and wind into account in addition to waves and tides. We also specified the sediment export in the tidal creeks, not in the salt marsh. Chongming Dongtan is primarily influenced by the sediment-rich Changjiang River and moderate tides, resulting in strong sedimentation.

4.3. Applicability, Limitations, and Prospects

The coupled flow-wave-sediment-vegetation model was developed with a perspective of general applicability in estuarine studies. The unstructured triangular grid used in the model could provide flexible geometric fitting for irregular tidal creeks and vegetation patches over various horizontal sizes. With sufficient computational resources, the model mesh could be refined to resolve subgrid dynamics. The model also includes the major physical properties of plant stems for different vegetation species with options for various parametrizations. This model could be applied to vegetated salt marshes in other estuaries with the proper specification of these plant properties.

The interactions among flows, waves, sediment, and vegetation are complex processes that involve various physical dynamics, parameterizations, and model implementations. Many model parameters used for sediments are mainly derived from flume experiments conducted with specific flows, sediments, and wave setups with scaled, finite water depths. In realistic conditions, these parameters have much broader ranges

under varying physical conditions. Taking $Q_s = \begin{cases} 2.15e^{-2.06/k_{t*}}, & k_{t*} < 0.95 \\ 0.27k_{t*}^3, & 0.95 < k_{t*} < 2.74 \end{cases}$ (Equation 11) from Yang and

Nepf (2018) as an example, to examine the bedload-mediated emergence of bedforms in vegetated channels, flume experiments were conducted with sandy sediment configurations. The sand diameters ranged from 0.42 to 0.60 mm, with a median grain size of 0.5 mm. The sediment parameters determined from these experiments are highly relevant to tidal channel conditions. However, when studying the impacts of sediment on lateral water exchanges between channels and adjacent mudflats, particle transport is expected to be governed by the fine cohesive fractions suspended in the water column (Green & Coco, 2007). These fine cohesive sediments can be transported by lower energy flows and modeled by an advection-diffusion equation under a balance between shear stress-dependent erosion and floc size-dependent settling velocities (Zhang et al., 2019). The cohesive sediment model has already been implemented as a default algorithm in the FVCOM sediment module (Ge et al., 2015).

It is also difficult to accurately simulate sediments in complex salt marsh and tidal creek regions. First, different criteria have been obtained for incipient sediment motion in creeks, bare mudflats, and vegetated marshes (Yang et al., 2016). These typical landscapes imply various bottom boundary conditions. The determination of incipient motion was based on the assumption of critical shear stress in bare mudflats while ignoring the effects of other variables, such as soil density, porosity, composition, consolidation status, sediment evolution, and the interactions among physical and biological processes. The critical shear stress for erosion in *Partheniades'* formula changes with water depth and bed properties. The bed soil in salt marshes has distinct characteristics among areas of different topographic elevations (Pieterse et al., 2016). Therefore,

it is a great challenge to parameterize bed properties in the salt marsh. Moreover, the microtopography in the salt marsh could limit the simulation precision for the wet/dry process and make it difficult to accurately capture fine-scale water transport (Wu et al., 2017).

Within tidal creeks, near-bed observations revealed high SSCs at the beginning of the flood tide and the end of the ebb tide (Figure 5d). The SSCs were much higher at the beginning of the flood tide than during the late period of the ebb tide, particularly during spring tidal cycles. The first sediment suspension peak was caused by bore-like flooding flows, which intensified the shear stress on the bed soil and caused massive erosion (Winterwerp & Van Kesteren, 2004). This process was typically nonhydrostatic. The FVCOM includes nonhydrostatic dynamics that can resolve this process; however, the module has not yet been expanded to take vegetation into account.

5. Conclusions

This study integrated TLS measurements, remote sensing data, field observations, and modeling to investigate tidal flows and lateral transport within the estuarine-salt marsh-tidal creek complex of Chongming Dongtan. A vegetation model was developed under the framework of the FVCOM to consider the impacts of multiple vegetation species on flows, turbulence, waves, and sediments. Three major vegetation types (*S. alterniflora*, *S. mariqueter*, and *P. australis*) were parameterized in the vegetation module. The model provided reasonable predictions of water levels, flow variations, sediments, and wet/dry processes in the studied salt marsh-tidal creek complex. The modeling results revealed and quantified the lateral fluxes between the salt marsh and tidal creeks. The widely distributed vegetation in the salt marsh greatly affected lateral transport. The comparison between the vegetated and nonvegetated cases indicated that vegetation can significantly delay and weaken flows in the salt marsh and enhance flows in low-elevation regions of tidal creeks.

Moreover, vegetation can significantly modify spatiotemporal variations in flows in the salt marsh, particularly at high tide during the spring tidal cycle. The simulated lateral transport varied considerably with salt marsh elevation, and the net flux either entering or outflowing from the major tidal creeks could not reach equilibrium over a 2-week time scale. Physiologically, *S. alterniflora* has a greater salt tolerance than *P. australis*. The simulated salinity distribution is consistent with the plant's salt tolerance, with high-salinity water present in the *S. alterniflora* area and low-salinity water present in the *P. australis* region. This suggests that lateral salinity transport not only redistributes salinity but also changes the evolution of vegetation coverage in salt marshes. The model predicts a significant net sediment export from the tidal creeks to the offshore region over the tidal cycle and high-SSC waters near the low-elevation creeks.

The flow-wave-vegetation-sediment interaction model was developed for general application. This model could be applied to wetland-tidal creek-salt marsh complexes with similar vegetation in other coastal and estuarine regions. It should be noted that this study is mainly focused on the lateral transport of water, salinity, and sediments between tidal creeks and salt marshes under calm weather conditions. These transport processes may differ significantly under extreme weather conditions, such as during tropical cyclones, storms, and typhoons/hurricanes. These modeling results obtained in the Changjiang River Estuary should be applied with caution when interpreting lateral transport processes in different estuarine environments.

Data Availability Statement

The flow-wave-sediment-vegetation interaction model used in this study was included in the latest FVCOM version 5.0, which is freely available (<http://code.fvcom.org/medm>). All datasets used in this work are publicly available at <https://doi.org/10.6084/m9.figshare.12424322.v1>.

Acknowledgments

This work was supported by the National Natural Science Foundation of China (Grant No. 41776104), the National Key R&D Program of China (Grant No. 2016YFA0600903), and the "Ecology+" Initiative of East China Normal University. C. Chen was supported by the Montgomery Charter Chair fund at the University of Massachusetts-Dartmouth. The authors express their thanks to Dr. Zhiyuan Zhao, who helped with the processing of the remote sensing data.

References

- Baptista, A., Zhang, Y., Chawla, A., Zulauf, M., Seaton, C., Myers Iii, E., et al. (2005). A cross-scale model for 3D baroclinic circulation in estuary-plume-shelf systems: II. Application to the Columbia River. *Continental Shelf Research*, 25(7–8), 935–972. <https://doi.org/10.1016/j.csr.2004.12.003>
- Beudin, A., Kalra, T. S., Ganju, N. K., & Warner, J. C. (2017). Development of a coupled wave-flow-vegetation interaction model. *Computers & Geosciences*, 100(C), 76–86. <https://doi.org/10.1016/j.cageo.2016.12.010>
- Boesch, D. F., & Turner, R. E. (1984). Dependence of fishery species on salt marshes: The role of food and refuge. *Estuaries*, 7(4), 460–468. <https://doi.org/10.2307/1351627>
- Chen, C., Beardsley, R., Cowles, G., Qi, J., Lai, Z., Gao, G., et al. (2013). An unstructured grid, finite-volume community ocean model FVCOM user manual. Retrieved from <http://fvcom.smast.umassd.edu/fvcom/>
- Chen, C., Liu, H., & Beardsley, R. C. (2003). An unstructured, finite-volume, three-dimensional, primitive equation ocean model: Application to coastal ocean and estuaries. *Journal of Atmospheric and Oceanic Technology*, 20, 159–186. [https://doi.org/10.1175/1520-0426\(2003\)020<0159:augfv>2.0.co;2](https://doi.org/10.1175/1520-0426(2003)020<0159:augfv>2.0.co;2)
- Chen, C., Qi, J., Li, C., Beardsley, R. C., Lin, H., Walker, R., & Gates, K. (2008). Complexity of the flooding/drying process in an estuarine tidal-creek salt-marsh system: An application of FVCOM. *Journal of Geophysical Research*, 113(C7), 469–521. <https://doi.org/10.1029/2007Jc004328>
- Cheng, X., Hou, L., Liu, M., Zheng, Y., Yin, G., Li, X., et al. (2015). Inorganic nitrogen exchange across the sediment-water interface in the eastern Chongming tidal flat of the Yangtze Estuary. *Environmental Earth Sciences*, 74(3), 2173–2184. <https://doi.org/10.1007/s12665-015-4207-z>
- Chiril, C. D., Haigh, I. D., Pontee, N., Thompson, C. E., & Gallop, S. L. (2018). Parametrizing tidal creek morphology in mature salt marsh using semi-automated extraction from lidar. *Remote Sensing of Environment*, 209, 291–311. <https://doi.org/10.1016/j.rse.2017.11.012>
- Chu, S. N., Wang, Z. A., Gonneea, M. E., Kroeger, K. D., & Ganju, N. K. (2018). Deciphering the dynamics of inorganic carbon export from intertidal salt marshes using high-frequency measurements. *Marine Chemistry*, 206, 7–18. <https://doi.org/10.1016/j.marchem.2018.08.005>
- Coco, G., Zhou, Z., Maanen, B., Van Olabarrieta, M., Tinoco, R., & Townend, I. (2013). Morphodynamics of tidal networks. *Marine Geology*, 346, pp. 1–16. <https://doi.org/10.1016/j.margeo.2013.08.005>
- Coleman, D. J., Ganju, N. K., & Kirwan, M. L. (2020). Sediment delivery to a tidal marsh platform is minimized by source decoupling and flux convergence. *Journal of Geophysical Research: Earth Surface*, 125(8), 151–213. <https://doi.org/10.1029/2020JF0055>
- Cui, L., Yuan, L., Ge, Z., Cao, H., & Zhang, L. (2020). The impacts of biotic and abiotic interaction on the spatial pattern of salt marshes in the Yangtze Estuary, China. *Estuarine, Coastal and Shelf Science*, 238, 106717. <https://doi.org/10.1016/j.ecss.2020.106717>
- D'Alpaos, L., Carniello, L., & Defina, A. (2019). Chapter 9-Mathematical modeling of tidal flow over salt marsh and tidal flats with applications to the venice lagoon (pp. 325–355). Elsevier. Coastal Wetlands. <https://doi.org/10.1016/B978-0-444-63893-9.000>
- De Serio, F., Ben Meftah, M., Mossa, M., & Termini, D. (2018). Experimental investigation on dispersion mechanisms in rigid and flexible vegetated beds. *Advances in Water Resources*, 120, 98–113. <https://doi.org/10.1016/j.advwatres.2017.08.005>
- Donatelli, C., Ganju, N. K., Fagherazzi, S., & Leonardi, N. (2018). Seagrass impact on sediment exchange between tidal flats and salt marsh, and the sediment budget of shallow bays. *Geophysical Research Letters*, 45(10), 4933–4943. <https://doi.org/10.1029/2018GL078056>
- Egbert, G. D., & Erofeeva, S. Y. (2002). Efficient inverse modeling of Barotropic Ocean tides. *Journal of Atmospheric and Oceanic Technology*, 19(2), 183–204. [https://doi.org/10.1175/1520-0426\(2002\)019<0183:eimobo>2.0.co;2](https://doi.org/10.1175/1520-0426(2002)019<0183:eimobo>2.0.co;2)
- Fagherazzi, S., Mariotti, G., Wiberg, P., & McGlathery, K. (2013). Marsh collapse does not require sea level rise. *Oceanography*, 26(3), 70–77. <https://doi.org/10.5670/oceanog.2013.47>
- Field, J. P., Breshears, D. D., Whicker, J. J., & Zou, C. B. (2012). Sediment capture by vegetation patches: Implications for desertification and increased resource redistribution. *Journal of Geophysical Research*, 117(G1), 273–279. <https://doi.org/10.1029/2011JG001663>
- Folkard, A. M. (2011). Vegetated flows in their environmental context: A review. *Proceedings of the Institution of Civil Engineers*, 164, 3–24. <https://doi.org/10.1680/j.eacm.8.00006>
- Ge, J., Chen, C., Wang, Z. B., Ke, K., Yi, J., & Ding, P. (2020). Dynamic response of the fluid mud to a tropical storm. *Journal of Geophysical Research-Oceans*, 125(3), 1–27. <https://doi.org/10.1029/2019JC015419>
- Ge, J., Ding, P., Chen, C., Hu, S., Fu, G., & Wu, L. (2013). An integrated East China Sea-Changjiang Estuary model system with aim at resolving multi-scale regional-shelf-estuarine dynamics. *Ocean Dynamics*, 63(8), 881–900. <https://doi.org/10.1007/s10236-013-0631-3>
- Ge, J., Shen, F., Guo, W., Chen, C., & Ding, P. (2015). Estimation of critical shear stress for erosion in the Changjiang Estuary: A synergy research of observation, GOCIsensing and modeling. *Journal of Geophysical Research-Oceans*, 120(12), 8439–8465. <https://doi.org/10.1002/2015JC010992>
- Ge, J., Zhou, Z., Yang, W., Ding, P., Chen, C., Wang, Z. B., & Gu, J. (2018). Formation of Concentrated Benthic Suspension in a Time-Dependent Salt Wedge Estuary. *Journal of Geophysical Research-Oceans*, 123(11), 8581–8607. <https://doi.org/10.1029/2018JC013876>
- Ge, Z. M., Zhang, L. Q., Yuan, L., & Zhang, C. (2014). Effects of salinity on temperature-dependent photosynthetic parameters of a native C3 and a non-native C4 marsh grass in the Yangtze Estuary, China. *Photosynthetica*, 52(4), 484–492. <https://doi.org/10.1007/s11099-014-0055-4>
- Geyer, W. R., (1993). The importance of suppression of turbulence by stratification on the estuarine turbidity maximum. *Estuaries*, 16(1), 113–125. <https://doi.org/10.2307/1352769>
- Green, M. O., & Coco, G. (2007). Sediment transport on an estuarine intertidal flat: Measurements and conceptual model of waves, rainfall and exchanges with a tidal creek. *Estuarine, Coastal and Shelf Science*, 72(4), 553–569. <https://doi.org/10.1016/j.ecss.2006.11.006>
- Green, M. O., & Hancock, N. J. (2012). Sediment transport through a tidal creek. *Estuarine, Coastal and Shelf Science*, 109, 116–132. <https://doi.org/10.1016/j.ecss.2012.05.030>
- Gulzar, S., Khan, M. A., & Ungar, I. A. (2007). Salt Tolerance of a coastal salt marsh grass. *Communications in Soil Science and Plant Analysis*, 34(17–18), 2595–2605. <https://doi.org/10.1081/CSS-120024787>
- Heuner, M., Silinski, A., Schoelynck, J., Bouma, T. J., Puijalon, S., Troch, P., et al. (2015). Ecosystem engineering by plants on wave-exposed intertidal flats is governed by relationships between effect and response traits. *PloS One*, 10(9), e0138086. <https://doi.org/10.1371/journal.pone.0138086>
- Houwing, E. (1999). Determination of the critical erosion threshold of cohesive sediments on intertidal mudflats along the Dutch Wadden Sea coast. *Estuarine, Coastal and Shelf Science*, 49(4), 545–555. <https://doi.org/10.1006/ecss.1999.0518>
- Hu, K., Chen, Q., & Wang, H. (2015). A numerical study of vegetation impact on reducing storm surge by wetlands in a semi-enclosed estuary. *Coastal Engineering*, 95(C), 66–76. <https://doi.org/10.1016/j.coastaleng.2014.09.008>

- Huang, H., & Zhang, L. (2007). A study of the population dynamics of *Spartina alterniflora* at Jiuduansha shoals, Shanghai, China. *Ecological Engineering*, 29(2), 164–172. <https://doi.org/10.1016/j.ecoleng.2006.06.005>
- Karan, S. K., & Samadder, S. R. (2016). Accuracy of land use change detection using support vector machine and maximum likelihood techniques for open-cast coal mining areas. *Environmental Monitoring and Assessment*, 188(8), 486. <https://doi.org/10.1007/s10661-016-5494-x>
- Katul, G. G., Poggi, D., & Ridolfi, L. (2011). A flow resistance model for assessing the impact of vegetation on flood routing mechanics. *Water Resources Research*, 47(8), 1107–1115. <https://doi.org/10.1029/2010WR010278>
- Kirwan, M. L., Murray, A. B., Donnelly, J. P., & Corbett, D. R. (2011). Rapid wetland expansion during European settlement and its implication for marsh survival under modern sediment delivery rates. *Geology*, 39(5), 507–510. <https://doi.org/10.1130/G31789.1>
- Klopstra, D., Barneveld, H. J., Van Noortwijk, J. M., & Van Velzen, E. H. (1997). Analytical model for hydraulic roughness of submerged vegetation. In Proc Managing Water (Ed.), *Coping with scarcity and abundance* (p. 775). ASCE.
- Lacy, J. R., Ferner, M. C., & Callaway, J. C. (2018). The influence of neap-spring tidal variation and wave energy on sediment flux in salt marsh tidal creeks. *Earth Surface Processes and Landforms*, 43, 2384–2396. <https://doi.org/10.1002/esp.4401>
- Ladd, C. J. T., Edwards, D. M. F., Bouma, T. J., Pagès, J. F., & Skov, M. W. (2019). Sediment supply explains long-term and large-scale patterns in salt marsh lateral expansion and erosion. *Geophysical Research Letters*, 46(20), 11178–11187. <https://doi.org/10.1029/2019gl083315>
- Lai, Z., Ma, R., Gao, G., Chen, C., & Beardsley, R. C., (2015). Impact of multichannel river network on the plume dynamics in the Pearl River estuary. *Journal of Geophysical Research-Oceans*, 120(8), 5766–5789. <https://doi.org/10.1002/2014JC010490>
- Larsen, L. G. (2019). Multiscale flow-vegetation-sediment feedbacks in low-gradient landscapes. *Geomorphology*, 334(C), 165–193. <https://doi.org/10.1016/j.geomorph.2019.03.009>
- Leonard, L. A., & Reed, D. J. (2002). Hydrodynamics and sediment transport through tidal marsh canopies. *Journal of Coastal Research*, 459–469.
- Leonardi, N., Defne, Z., Ganju, N. K., & Fagherazzi, S. (2016). Salt marsh erosion rates and boundary features in a shallow bay. *Journal of Geophysical Research: Earth Surface*, 121, 1861–1875. <https://doi.org/10.1002/2016jef003975>
- Li, S.-H., Ge, Z.-M., Xie, L.-N., Chen, W., Yuan, L., Wang, D.-Q., et al. (2018). Ecophysiological response of native and exotic salt marsh vegetation to waterlogging and salinity: Implications for the effects of sea-level rise. *Scientific Reports*, 8, 1–13. <https://doi.org/10.1038/s41598-017-18721-z>
- Li, X., Leonardi, N., & Plater, A. J. (2019). Wave-driven sediment resuspension and salt marsh frontal erosion alter the export of sediments from macro-tidal estuaries. *Geomorphology*, 325(C), 17–28. <https://doi.org/10.1016/j.geomorph.2018.10.004>
- Li, X., Plater, A., & Leonardi, N. (2018). Modelling the transport and export of sediments in macrotidal estuaries with eroding salt marsh, estuaries and coasts. *Estuaries and Coasts*, 1–14. <https://doi.org/10.1007/s12237-018-0371-1>
- Liu, C., & NEPF, H. (2016). Sediment deposition within and around a finite patch of model vegetation over a range of channel velocity. *Water Resources Research*, 52(1), 600–612. <https://doi.org/10.1002/2015WR018249>
- Luan, H. L., Ding, P.-X., Wang, Z. B., Ge, J.-Z., & Yang, S.-L. (2016). Decadal morphological evolution of the Yangtze Estuary in response to river input changes and estuarine engineering projects. *Geomorphology*, 265, 12–23. <https://doi.org/10.1016/j.geomorph.2016.04.022>
- Luhar, M., Coutu, S., Infantes, E., Fox, S., & NEPF, H. (2010). Wave-induced velocities inside a model seagrass bed. *Journal of Geophysical Research*, 115, F01004. <https://doi.org/10.1029/2010JC006345>
- Luhar, M., & Nepf, H. M. (2011). Flow-induced reconfiguration of buoyant and flexible aquatic vegetation. *Limnology & Oceanography*, 56(6), 2003–2017. <https://doi.org/10.4319/lo.2011.56.6.2003>
- Luhar, M., & Nepf, H. M. (2013). From the blade scale to the reach scale: A characterization of aquatic vegetative drag. *Advances in Water Resources*, 51, 305–316. <https://doi.org/10.1016/j.advwatres.2012.02.002>
- Ma, G., Han, Y., Niroomandi, A., Lou, S., & Liu, S. (2014). Numerical study of sediment transport on a tidal flat with a patch of vegetation. *Ocean Dynamics*, 65(2), 203–222. <https://doi.org/10.1007/s10236-014-0804-8>
- Mariotti, G. (2018). Marsh channel morphological response to sea level rise and sediment supply. *Estuarine, Coastal and Shelf Science*, 209, 89–101. <https://doi.org/10.1016/j.ecss.2018.05.016>
- Mariotti, G., & Fagherazzi, S. (2012). Channels-tidal flat sediment exchange: The channel spillover mechanism. *Journal of Geophysical Research*, 117. <https://doi.org/10.1029/2011jc007378>
- Mariotti, G., & Fagherazzi, S. (2013). A two-point dynamic model for the coupled evolution of channels and tidal flats. *Journal of Geophysical Research: Earth Surface*, 118(3), 1387–1399. <https://doi.org/10.1002/jgrf.20070>
- Marsooli, R., & Wu, W. (2014). Numerical investigation of wave attenuation by vegetation using a 3D RANS model. *Advances in Water Resources*, 74(C), 245–257. <https://doi.org/10.1016/j.advwatres.2014.09.012>
- McOwen, C., Weatherdon, L., Bochove, J.-W., Sullivan, E., Blyth, S., Zockler, C., et al. (2017). A global map of salt marsh. *Biodiversity Data Journal*, 5, e11764–13. <https://doi.org/10.3897/BDJ.5.e11764>
- Mellor, G. L., & Yamada, T. (1982). Development of a turbulence closure model for geophysical fluid problem. *Reviews of Geophysics and Space Physics*, 20, 851–875. <https://doi.org/10.1029/rg020i004p00851>
- Morris, J. T., Sundareshwar, P. V., Nietch, C. T., Kjerfve, B., & Cahoon, D. R. (2002). Responses of coastal wetlands to rising sea level. *Ecology*, 83(10), 2869–2877. [https://doi.org/10.1890/0012-9658\(2002\)083\[2869:rocwtr\]2.0.co;2](https://doi.org/10.1890/0012-9658(2002)083[2869:rocwtr]2.0.co;2)
- Munk, W. H., & Anderson, E. R. (1948). Notes on the theory of the thermocline. *Journal of Marine Research*, 7, 276–295.
- Nepf, H. M. (1999). Drag, turbulence, and diffusion in flow through emergent vegetation. *Water Resources Research*, 35(2), 479–489. <https://doi.org/10.1029/1998WR900069>
- Nepf, H. M. (2012). Flow and transport in regions with aquatic vegetation. *Annual Review of Fluid Mechanics*, 44(1), 123–142. <https://doi.org/10.1146/annurev-fluid-120710-101048>
- Nepf, H. M., & Vivoni, E. R. (2000). Flow structure in depth-limited, vegetated flow. *Journal of Geophysical Research-Oceans*, 105(C), 28547–28557. <https://doi.org/10.1029/2000JC900145>
- Niu, Q., & Xia, M. (2017). The role of wave-current interaction in Lake Erie's seasonal and episodic dynamics. *Journal of Geophysical Research: Oceans*, 122(9), 7291–7311. <https://doi.org/10.1002/2017jc012934>
- Partheniades, E. (1965). Erosion and Deposition of Cohesive Soils. *Journal of Hydraulic Engineering*, 91, 105–139. <https://doi.org/10.1061/jyceaj.0001165>
- Pieterse, A., Puleo, J. A., & McKenna, T. E. (2016). Hydrodynamics and sediment suspension in shallow tidal channels intersecting a tidal flat. *Continental Shelf Research*, 119, 40–55. <https://doi.org/10.1016/j.csr.2016.03.012>

- Poepl, R. E., Keiler, M., Von elverfeldt, K., Zweimueller, I., & Glade, T. (2016). The influence of riparian vegetation cover on diffuse lateral sediment connectivity and biogeomorphic processes in a medium-sized agricultural catchment, Austria. *Geografiska Annaler - Series A: Physical Geography*, 94(4), 511–529. <https://doi.org/10.1111/j.1468-0459.2012.00476.x>
- Poirier, E., van Proosdij, D., & Milligan, T. G. (2017). The effect of source suspended sediment concentration on the sediment dynamics of a macrotidal creek and salt marsh. *Continental Shelf Research*, 148, 130–138. <https://doi.org/10.1016/j.csr.2017.08.017>
- Qi, J., Chen, C., Beardsley, R. C., Perrie, W., Cowles, G. W., & Lai, Z. (2009). An unstructured-grid finite-volume surface wave model (FVCOM-SWAVE): Implementation, validations and applications. *Ocean Modelling*, 28(1), 153–166. <https://doi.org/10.1016/j.ocemod.2009.01.007>
- Riegl (2019). *Riegl VZ-4000 specifications*. Retrieved from http://riegl.com/uploads/tx_pxpriegl/downloads
- Schuerch, M., Dolch, T., Reise, K., & Vafeidis, A. T. (2014). Unravelling interactions between salt marsh evolution and sedimentary processes in the Wadden Sea (southeastern North Sea). *Progress in Physical Geography: Earth and Environment*, 38(6), 691–715. <https://doi.org/10.1177/0309133314548746>
- Serra, T., Fernando, H. J. S., & Rodríguez, R. V. (2004). Effects of emergent vegetation on lateral diffusion in wetlands. *Water Research*, 38(1), 139–147. <https://doi.org/10.1016/j.watres.2003.09.009>
- Shi, B., Cooper, J. R., Pratalongo, P. D., Gao, S., Bouma, T. J., Li, G., et al. (2017a). Erosion and accretion on a Mudflat: The importance of very shallow-water effects. *Journal of Geophysical Research-Oceans*, 122(12), 9476–9499. <https://doi.org/10.1002/2016jc012316>
- Shi, B. W., Yang, S. L., Wang, Y. P., Li, G. C., Li, M. L., Li, P., & Li, C. (2017b). Role of wind in erosion-accretion cycles on an estuarine mudflat. *Journal of Geophysical Research Oceans*, 122, 193–206. <https://doi.org/10.1002/2016jc011902>
- Stefanon, L., Carniello, L., D'Alpaos, A., & Lanzoni, S. (2010). Experimental analysis of tidal network growth and development. *Continental Shelf Research*, 30(8), 950–962. <https://doi.org/10.1016/j.csr.2009.08.018>
- Tal, M., & Paola, C. (2010). Effects of vegetation on channel morphodynamics: Results and insights from laboratory experiments. *Earth Surface Processes and Landforms*, 35(9), 1014–1028. <https://doi.org/10.1002/esp.1908>
- Tanino, Y., & Nepf, H. M. (2008). Lateral dispersion in random cylinder arrays at high Reynolds number. *Journal of Fluid Mechanics*, 600, 339–371. <https://doi.org/10.1017/s0022112008000505>
- Temmerman, S., Bouma, T. J., Govers, G., Wang, Z. B., Vries, D. M. B., & Herman, P. M. J. (2005). Impact of vegetation on flow routing and sedimentation patterns: Three-dimensional modeling for a tidal marsh. *Journal of Geophysical Research*, 110. <https://doi.org/10.1029/2005JF000301>
- Temmerman, S., Moonen, P., Schoelynck, J., Govers, G., & Bouma, T. J. (2012). Impact of vegetation die-off on spatial flow patterns over a tidal marsh. *Geophysical Research Letters*, 39. <https://doi.org/10.1029/2011GL050502>
- Tinoco, R. O., & Coco, G. (2018). Turbulence as the main driver of resuspension in oscillatory flow through vegetation. *Journal of Geophysical Research: Earth Surface*, 123(5), 891–904. <https://doi.org/10.1002/2017JF004504>
- Uittenbogaard, R. (2003). Modelling turbulence in vegetated aquatic flowshydraulic, morphological and ecological aspects, Trento. *International workshop on Riparian Forest vegetated channels*, 20–22.
- Vélez-Martín, A., Davy, A. J., Luque, C. J., & Castellanos, E. M. (2020). Disentangling elevation, annual flooding regime and salinity as hydrochemical determinants of halophyte distribution in non-tidal salt marsh. *Annals of Botany*, 126(2), 277–288. <https://doi.org/10.1093/aob/mcaa078>
- Verschelling, E., van der Deijl, E., van der Perk, M., Sloff, K., & Middelkoop, H. (2017). Effects of discharge, wind, and tide on sedimentation in a recently restored tidal freshwater wetland. *Hydrological Processes*, 31(16), 2827–2841. <https://doi.org/10.1002/hyp.11217>
- Wang, C., Yao, D., He, B., Zhou, N., & Xu, S. (2011). Cross-shore suspended sediment flux in the salt marsh pioneer zone of Chongming eastern beach in the Changjiang Estuary in China. *Acta Oceanologica Sinica*, 29(6), 62–72. <https://doi.org/10.1007/s13131-010-0077-0>
- Wang, Z. A., Kroeger, K. D., Ganju, N. K., Gonnea, M. E., & Chu, S. N. (2016). Intertidal salt marshes as an important source of inorganic carbon to the coastal ocean. *Limnology & Oceanography*, 61(5), 1916–1931. <https://doi.org/10.1002/lno.10347>
- Warner, J., Sherwood, C., Signell, R., Harris, C., & Arango, H. (2008). Development of a three-dimensional, regional, coupled wave, current, and sediment-transport model. *Computers and Geosciences*, 34(10), 1284–1306.
- Wiberg, P. L., Fagherazzi, S., & Kirwan, M. L. (2020). Improving predictions of salt marsh evolution through better integration of data and models. *Annual Review of Marine Science*, 12(1), 389–413. <https://doi.org/10.1146/annurev-marine-010419-010610>
- Willmott, C. J. (1981). On the validation of models. *Physical Geography*, 2(2), 184–194. <https://doi.org/10.1080/02723646.1981.10642213>
- Winterwerp, J., & Van Kesteren, W. (2004). *Introduction to the physics of cohesive sediment in the marine environment, developments in sedimentology* 56.
- Wu, G., Li, H., Liang, B., Shi, F., Kirby, J. T., & Mieras, R. (2017). Subgrid modeling of salt marsh hydrodynamics with effects of vegetation and vegetation zonation. *Earth Surface Processes and Landforms*, 42(12), 1755–1768. <https://doi.org/10.1002/esp.4121>
- Wu, L., Chen, C., Guo, P., Shi, M., Qi, J., & Ge, J. (2011). A FVCOM-based unstructured grid wave, current, sediment transport model, I. Model description and validation. *Journal of Ocean University of China*, 10(1), 1–8. <https://doi.org/10.1007/s11802-011-1788-3>
- Xie, W., He, Q., Wang, X., Guo, L., & Zhang, K. (2018). Role of mudflat-creek sediment exchanges in intertidal sedimentary processes. *Journal of Hydrology*, 567, 351–360. <https://doi.org/10.1016/j.jhydrol.2018.10.027>
- Xie, W., He, Q., Zhang, K., Guo, L., Wang, X., Shen, J., & Cui, Z. (2017). Application of terrestrial laser scanner on tidal flat morphology at a typhoon event timescale. *Geomorphology*, 292, 47–58. <https://doi.org/10.1016/j.geomorph.2017.04.034>
- Xue, P., Chen, C., Ding, P., Beardsley, R. C., Lin, H., Ge, J., & Kong, Y. (2009). Saltwater intrusion into the Changjiang River: A model-guided mechanism study. *Journal of Geophysical Research*, 114. <https://doi.org/10.1029/2008JC004831>
- Yang, J. Q., Chung, H., & Nepf, H. M. (2016). The onset of sediment transport in vegetated channels predicted by turbulent kinetic energy. *Geophysical Research Letters*, 43(2). <https://doi.org/10.1002/2016GL071092>
- Yang, J. Q., & Nepf, H. M. (2018). A turbulence-based bed-load transport model for bare and vegetated channels. *Geophysical Research Letters*, 45(19), 10428–10436. <https://doi.org/10.1029/2018gl079319>
- Yang, S. L., Ding, P. X., & Chen, S. L. (2001). Changes in progradation rate of the tidal flats at the mouth of the Changjiang (Yangtze) River, China. *Geomorphology*, 38(1–2), 167–180. [https://doi.org/10.1016/S0169-555X\(00\)00079-9](https://doi.org/10.1016/S0169-555X(00)00079-9)
- Yang, S. L., Fan, J. Q., Shi, B. W., Bouma, T. J., Xu, K. H., Yang, H. F., et al. (2019). Remote impacts of typhoons on the hydrodynamics, sediment transport and bed stability of an intertidal wetland in the Yangtze Delta. *Journal of Hydrology*, 575, 755–766. <https://doi.org/10.1016/j.jhydrol.2019.05.077>
- Yang, Z., Bai, F., Huai, W., An, R., & Wang, H. (2017). Modelling open-channel flow with rigid vegetation based on two-dimensional shallow water equations using the lattice Boltzmann method. *Ecological Engineering*, 106, 75–81. <https://doi.org/10.1016/j.ecoleng.2017.05.039>

- Yu, Q., Wang, Y., Shi, B., Wang, Y. P., & Gao, S. (2017). Physical and sedimentary processes on the tidal flat of central Jiangsu Coast, China_ Headland induced tidal eddies and benthic fluid mud layers. *Continental Shelf Research*, 133(C), 26–36. <https://doi.org/10.1016/j.csr.2016.12.015>
- Yuan, L., Ge, Z., Fan, X., & Zhang, L. (2014). Ecosystem-based coastal zone management: A comprehensive assessment of coastal ecosystems in the Yangtze Estuary coastal zone. *Ocean & Coastal Management*, 95(C), 63–71. <https://doi.org/10.1016/j.ocecoaman.2014.04.005>
- Yuan, L., Zhang, L., Xiao, L., & Huang, H., (2011). The application of cutting plus waterlogging to control *Spartina alterniflora* on salt-marshes in the Yangtze Estuary, China. *Estuarine, Coastal and Shelf Science*, 92(1), 103–110. <https://doi.org/10.1016/j.ecss.2010.12.019>
- Zhang, X., Leonardi, N., Donatelli, C., & Fagherazzi, S. (2019). Fate of cohesive sediments in a marsh-dominated estuary. *Advances in Water Resources*, 125, 32–40. <https://doi.org/10.1016/j.advwatres.2019.01.003>
- Zhao, L., Chen, C., Vallino, J., Hopkinson, C., Beardsley, R. C., Lin, H., & Lerczak, J. (2010). Wetland-estuarine-shelf interactions in the plum island sound and Merrimack River in the Massachusetts coast. *Journal of Geophysical Research*, 115(C10), 544–613. <https://doi.org/10.1029/2009JC006085>
- Zheng, Z., Zhou, Y., & Jiang, X., (2007). Integration of remote sensing technique and hydrologic model for monitoring tidal flat dynamics of Juiduansha in Shanghai. In W Ju & S Zhao(Eds.), (Vol. 6752, pp. 67522B). *Presented at the Geoinformatics 2007, SPIE*. <https://doi.org/10.1117/12.760786>
- Zhou, Z., Ge, J., Wang, Z. B., Maren, D. S., Ma, J., & Ding, P., (2019). Study of lateral flow in a stratified tidal channel-shoal system: The importance of intratidal salinity variation. *Journal of Geophysical Research-Oceans*, 124(9), 6702–6719. <https://doi.org/10.1029/2019JC015307>
- Zhu, Z., Yang, Z., & Bouma, T. J. (2019). Biomechanical properties of marsh vegetation in space and time: Effects of salinity, inundation and seasonality. *Annals of Botany*, 83, 82–14. <https://doi.org/10.1093/aob/mcz063>